AIAA JOURNAL
Vol. 62, No. 8, August 2024

Direct-Noise of an Ultrahigh-Bypass-Ratio Turbofan: Periodic-Sector vs Full-Annulus Large-Eddy Simulations

Jean Al-Am,* Alexis Giauque,† Vincent Clair,† and Jérôme Boudet†
Ecole Centrale de Lyon, CNRS, Universite Claude Bernard Lyon 1, INSA Lyon, LMFA, UMR5509, 69130 Ecully, France
and
Fernando Gea-Aguilera‡
Safran Aircraft Engines, 77550 Moissy-Cramayel, France

https://doi.org/10.2514/1.J063596

The tonal and broadband noise of an ultrahigh-bypass-ratio fan stage, which has been developed at École Centrale de Lyon, is studied using large-eddy simulations (LES). Wall-modeled LES of a periodic sector and a 360-deg full fan stage have been performed at approach conditions, which is a relevant operating point for aircraft noise certifications. The fan noise is directly obtained from the fully compressible LES, using a well-refined unstructured mesh, and compared with state-of-the-art analytical models. The impact of the periodic boundary conditions, which are often used for high-fidelity simulations of turbofan engines, is assessed. The results from the 360-deg and periodic-sector LES are compared from aerodynamic and acoustic perspectives, including an analysis of the mean and turbulent flow quantities and sound-pressure spectra. Aerodynamic parameters show similar results for both configurations. However, the fan blade loading is slightly reduced in the 360-deg- LES near the blade tip. Acoustically, lower sound power levels at the intake and exhaust sections of the fan stage are obtained in the 360-deg LES, when compared to the periodic sector LES, particularly at low and middle frequencies. This can be associated with lower coherence levels in the fan wakes and smaller spanwise correlation lengths at the trailing edge of the blades. The modal content of the acoustic field has also been analyzed in detail and shows that the periodic sector LES cannot correctly simulate the modal content of the fan noise.

Nomenclature

A^+_{mj}	=	modal amplitude of downstream propagating waves
A^-_{mj}	=	modal amplitude of upstream propagating waves
ANCF	=	advanced noise-control fan
B	=	fan blade count
BPF	=	blade-passing frequency, Hz
CPU	=	central processing unit
c_r	=	fan chord length, m
c_s	=	OGV chord length, m
c_0	=	speed of sound, m/s
f	=	frequency, Hz
f_c	=	cutoff frequency, Hz
f_{mj}	=	normalized modal radial function
I_a	=	acoustic intensity, W/m^2
i	=	imaginary unit
j	=	radial order
K_{mj}	=	eigenvalue of the duct mode (m, j)
k_{mj}	=	axial wavenumber of the duct mode (m, j), m^{-1}
k_z	=	spanwise wavenumber, m^{-1}
k_t	=	turbulent kinetic energy, m^2/s^2
LBM	=	lattice Boltzmann method
LES	=	large-eddy simulation
l_z	=	spanwise correlation length, m
M	=	Mach number
M_{is}	=	isentropic Mach number
m	=	azimuthal order
$\dot{m}$	=	mass flow rate, kg/sn = BPF harmonic order
OGV	=	outlet guide vane
P	=	static pressure, Pa
P_0	=	total pressure, Pa
p'	=	pressure fluctuations, Pa
Q	=	Q-criterion
RANS	=	Reynolds-averaged Navier–Stokes
Re	=	Reynolds number
R_h	=	hub radius, m
R_s	=	shroud radius, m
rmsRSI	=	rotor–stator interaction
rms	=	root mean square
SDT	=	source diagnostic test
SWL	=	sound power level, dB
s	=	integer
T_0	=	total temperature, K
TTGC	=	two-step Taylor Galerkin convection
t	=	time, s
U	=	velocity magnitude, m/s
UHBR	=	ultrahigh bypass ratio
u	=	streamwise velocity component, m/s
$\overline{u}$	=	moving average of a velocity component, m/s
u^+	=	dimensionless velocity in wall units
u'_{rms}	=	rms velocity fluctuations, m/s
V	=	stator vane count
V_x, V_r, V_θ	=	axial velocity component, radial velocity component, azimuthal velocity component, m/s
ν	=	kinematic viscosity, m^2/s
W_a	=	acoustic power, W
WM	=	wall modeled
x, y, z	=	axial, transverse, and spanwise directions, m
$\beta = \sqrt{1 - M^2}$	=	compressibility factor
γ	=	ratio of specific heats
γ^2	=	coherence
Δt	=	time step, s
Δz	=	spanwise distance, m

Received 24 September 2023; revision received 22 February 2024; accepted for publication 23 February 2024; published online 27 May 2024.

*R&D Aero-Acoustics Engineer, Aerodynamics and Acoustics Department, 77550 Moissy-Cramayel; Central Lyon and Safran; currently XX, Centrale School of Lyon, INSA Lyon, LMFA, UMR5509; jean.al-am@safrangroup.com.

†Professor, Ecole Centrale de Lyon, 36 avenue Guy de Collongue, F-69134, Ecully Cedex; Centrale School of Lyon, INSA Lyon, LMFA, UMR5509.

‡R&D Aero-Acoustics Engineer, Aerodynamics and Acoustics Department.

$\Delta x^+, \Delta y^+, \Delta z^+$	=	dimensionless wall distances
λ	=	turbulence length scale, m
λ_{ac}	=	acoustic wavelength, m
λ_{Ta}	=	Taylor microscale, m
ϵ	=	turbulent dissipation rate, m^2/s^3
ρ	=	density, kg/m^3
ρ_0	=	freestream density, kg/m^3
Φ_{pp}	=	power spectral density of wall-pressure fluctuations, Pa^2/Hz
Φ_{uu}	=	power spectral density of streamwise velocity fluctuations, m^2/s
Ω	=	rotation speed, rpm
Ω_n	=	nominal rotation speed, rpm
ω	=	angular frequency, $rad \cdot s^{-1}$
ω_c	=	cutoff angular frequency, $rad \cdot s^{-1}$

I. Introduction

TO COMPLY with international aviation regulations, aeroengine manufacturers optimize turbofan engines to improve efficiency while reducing CO_2 and noise emissions. To this end, modern aeroengines, such as ultrahigh bypass ratio (UHBR) turbofan engines, present an increased bypass ratio and a large fan diameter. For such turbofan engines, the fan/outlet guide vane (OGV) stage is one of the main noise sources [1]. The noise from the fan/OGV stage is usually characterized by tonal and broadband noise components. Tonal noise, which occurs at the blade-passing frequency (BPF), and its multiples, mainly arises from periodic interactions in the fan stage and depends on the blade and vane counts. The fan tonal noise is well addressed in the literature [1], and many solutions have been proposed to reduce tonal noise, such as the use of acoustic liners [2] in the inlet and exhaust ducts, and the optimization of the blade and vane counts to reduce interaction tones [3]. The broadband noise arises from different stochastic mechanisms in the fan stage and is less documented. The main broadband noise mechanisms in a fan stage are the blade-tip-leakage vortex noise, the trailing- edge noise, the separation noise, and the rotor–stator (RSI) interaction noise. The blade-tip-leakage vortex noise is generated by the interaction of the highly unsteady flow from the tip clearance with the trailing edge of the tip section and the neighboring blades [4]. The trailing-edge noise is generated by the diffraction of the turbulent boundary layers at the trailing edge of the fan blades and OGVs [5]. At low fan speeds, separation noise may occur, which results from an increased angle of attack and flow separation that leads to large pressure fluctuations close to the leading edge of the fan blade [6]. The RSI noise is generated by the interaction of turbulence in the fan wakes with the leading edges of the OGVs [7], which generates an unsteady loading on the vanes. The RSInoise is usually considered to be the dominant noise source of the fan stage at approach condition [8,9]. Over the past decades, several techniques have been developed to model and predict broadband noise from a fan stage [1,10].

Today, high-fidelity simulations, such as large-eddy simulation (LES), can be applied for turbomachinery applications due to the recent progress in computing resources. These numerical simulations allow for a detailed description of the turbulent structures that produce broadband noise. In the present study, LES is used to accurately model both the complex turbulent flow and the noise from the fan stage, at an acceptable computational expense.

To reduce the computational cost, a periodic sector has usually been considered in the previous numerical studies in the literature to analyze the broadband noise from a fan/OGV stage [1,11–13]. This type of numerical simulation is usually coupled with an analytical model [14,15] or an acoustic analogy [11,12,16], such as the Ffowcs Williams and Hawkings analogy [17] or the Goldstein analogy [18], to compute the acoustic field from the unsteady loadings on the surfaces of the blades and vanes. A good agreement was found between the noise predictions using these approaches and available experimental data. However, analytical models informed by numerical data usually underestimate the noise, whereas the hybrid approach based on an acoustic analogy is known to overestimate the noise levels [12]. In fully compressible LES, the acoustic power can also be directly obtained from the computational domain upstream and downstream of the fan stage, if the numerical setup is well adapted for the propagation of acoustic waves. A good agreement was obtained between direct noise predictions from a periodic fan/OGV stage and analytical models [13]. To further reduce the computational cost, some studies have used simplified configurations of a periodic sector, such as linear cascades [19] or airfoils with a reduced span [6].

For all previous numerical studies, the impact of azimuthal periodic boundary conditions on the flowfield and noise has not been investigated. However, the use of azimuthal periodic boundary conditions is a major assumption in the numerical simulations and needs further analysis and validation. Some of the main concerns related to the use of azimuthal periodic boundary conditions are listed below.

First, a perfect correlation between flow quantities is imposed at the azimuthal boundaries due to the periodic boundary conditions. This may lead to an overprediction of the flow and acoustic correlations, mainly at low-to-middle frequencies.

Furthermore, the distribution of the acoustic energy over the different acoustic duct modes is influenced by the periodic boundary conditions. The duct modal content is important to identify the amplitudes, the frequencies, and the propagating directions of the dominant acoustic modes in the fan stage [20]. Using a periodic sector, only the cut-on azimuthal mode orders that are related to the periodic angular sector can propagate in the fan stage.

Moreover, the use of periodic boundary conditions usually requires a modification of the original vane count and OGV geometry to allow for the same angular extent of the rotor and the stator domains. Several techniques have been developed to ensure that the fan stage performance and the flowfield remain similar between the original and the modified configurations [21]. However, the geometrical modification is expected to have an impact on the noise, particularly on the RSI noise.

The main objective of the present study is to investigate the influence of periodic boundary conditions on the flowfield and the noise emissions. To this end, the flowfield and the acoustic propagation from a fan/OGV stage are analyzed using a 360-deg and a periodic-sector LES. The numerical setup has been designed to ensure 1) an adequate description of the turbulent structures in the boundary layers and the wakes, and 2) an accurate propagation of the acoustic waves in the fan stage up to 20 kHz. The present 360-deg LES is compared to a periodic-sector LES, which was performed previously by the authors [13], using the same configuration and numerical setup. Acoustic spectra from both LES computations are also compared to state-of-the-art analytical models for the prediction of RSI noise and trailing-edge noise. The 360-deg LES of a full fan/OGV stage is a unique calculation that is useful in obtaining an improved understanding of the fan noise and assessing numerical and analytical assumptions.

The paper is organized as follows. Section II shows the configuration and the numerical setup used for the LES. The numerical convergence is then assessed in Sec. III for the different LES performed in the present study. The flow topology and the pressure coherence in the fan wake are compared between the periodic sector and the 360-deg LES configurations in Sec. IV. Finally, the acoustic field is analyzed using both LES and compared to analytical models in Sec. V.

II. Numerical Setup

A. Computational Domain

The configuration used in the present study is the ECL5 fan stage, which has been designed at Ecole Centrale de Lyon [22] using technical requirements for a midrange commercial aircraft. The ECL5 fan stage is a new open test case [23,24], which corresponds to a UHBR aeroengine model with a low rotational speed and without core flow. This advanced experiment is already supporting research on blade vibrations [25] and turbomachinery flow stability [26]. The ECL5 fan stage is composed of $B = 16$ fan blades and $V = 31$ OGVs.

The computational domains of the 360-deg and the periodic-sector configurations are presented in Fig. 1. The same angular extent for

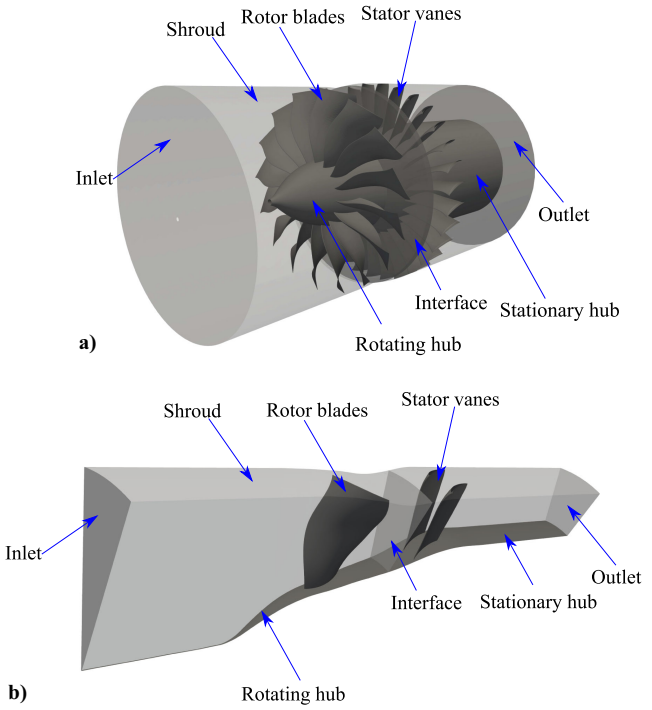

Fig. 1 Computational domains of a) the 360-deg, and b) the periodic-sector ECL5 fan stage.

the rotor and stator domains is required by the AVBP solver [27]. Consequently, the vane count is increased to 32 OGVs to allow for a $2\pi/16$ angular periodicity in the periodic-sector configuration. In this case, the OGV chord length is adjusted to keep the solidity, which is defined as the ratio between the chord length and the intervane spacing. This is useful to maintain the stage performance [21]. The computational domain extends from 3.75 fan chord length c_r, upstream of the fan leading edge, to 4.25 vane chord length c_s, downstream of the OGV trailing edge. The distance upstream of the fan is chosen to ensure a well-developed boundary layer on the outer casing. The tip clearance is set to 0.965 mm at the leading edge and 1.27 mm at the trailing edge of the fan blade.

The present simulations are performed at approach conditions with a rotational speed of $\Omega = 6050$ rpm, which corresponds to 55% of the nominal rotational speed Ω_n, using the fan hot shape. At this operating condition, the inflow axial Mach number is about 0.3 and the relative Mach number at the blade tip is 0.56. Thus, the fan operates in a fully subsonic regime at approach conditions. The Reynolds number based on the rotor midspan chord length is approximately 10^6.

The fan stage performance obtained from both LES are compared with some available experimental data obtained from the ECL5 fan stage at approach condition. The mass flow rate $\dot{m}$, the total pressure ratio, and the isentropic efficiency, obtained from both LES and experimental campaign, are compared in Table 1. These values were obtained from a mass-flow rate weighted average over axial field cuts upstream of the fan and downstream of the OGV. Both LES results show good agreement with the experiment data, where small discrepancies are noted for the mass flow rate (−0.1%), the total pressure ratio (0.57% for the periodic sector LES and 0.41% for the 360-deg LES), and the isentropic efficiency (−0.42% for the periodic sector LES and −0.26% for the 360-deg LES).

Table 1 Fan-stage performance at approach condition

	Experiment	Sector LES	360-deg LES
$\dot{m}$ [kg/s]	22.00	21.97	21.98
Total-pressure ratio	1.0863	1.0801 (−0.57%)	1.0819 (−0.41%))
isentropic efficiency	0.9072	0.9034 (−0.42%)	0.9048 (−0.26%)

B. LES Setup

The LES governing equations are solved using the AVBP solver [27]. AVBP is an explicit, unstructured, fully compressible LES solver, which has been developed by Centre Européen de Recherche et de Formation Avancée en Calcul Scientifique [27]. Two LES domains, which correspond to the rotor and stator domains, are coupled using CWIPI, which is based on an overlapping grid method [28]. The rotor domain contains the fan blades, and the stator domain contains the OGVs.

Two-step Taylor–Galerkin convective scheme is used to solve the filtered Navier–Stokes equations [29], which is a third-order finite-volume convective scheme. The unresolved turbulent eddies are modeled using the SIGMA subgrid scale model [30]. At the inlet and outlet sections, nonreflecting Navier–Stokes Characteristic Boundary Conditions [31] are used. A uniform mean flow is injected at the inlet section in the axial direction, with a total pressure of $P_0 = 101325$ Pa and a total temperature of $T_0 = 300$ K. The static pressure is adjusted at the outlet section to obtain the target mass flow rate in the fan stage. For the periodic-sector configuration, periodic boundary conditions are used on the azimuthal boundaries of the computational domain. On the wall surfaces of the blades, vanes, and shroud and hub, a no-slip boundary condition is used. A wall law [32] is used to model the inner part of the boundary layer. A dimensionless velocity relative to the wall $u^+ = (1/\kappa)\,\ell_n(A\Delta y^+)$ for $\Delta y^+ > 11.45$, with $\kappa = 0.41$ and $A = 9.2$, is adopted. Below $\Delta y^+ = 11.45$, a linear wall law is imposed.

The time step for the simulations is set to $\Delta t = 2.8 \times 10^{-8}$ s and the computational cost is approximately 105×10^3 CPUh per rotation for the periodic-sector configuration and 1700×10^3 CPUh per rotation for the 360-deg configuration. Two full-fan rotations have been performed for the numerical convergence, and four additional fan rotations were performed for the postprocessing and acoustic data collection.

C. Mesh Characteristics

The mesh at midspan around the rotor blades and stator vanes is shown in Fig. 2. The same mesh structure is used for both the periodic sector and the 360-deg LES configurations. The unstructured hybrid mesh is composed of different types of elements. Prismatic cells are used on the solid surfaces, including the blades, vanes, shroud and hub, tetrahedral cells away from the solid surfaces, and pyramidal cells in the transition region between prismatic and tetrahedral cells.

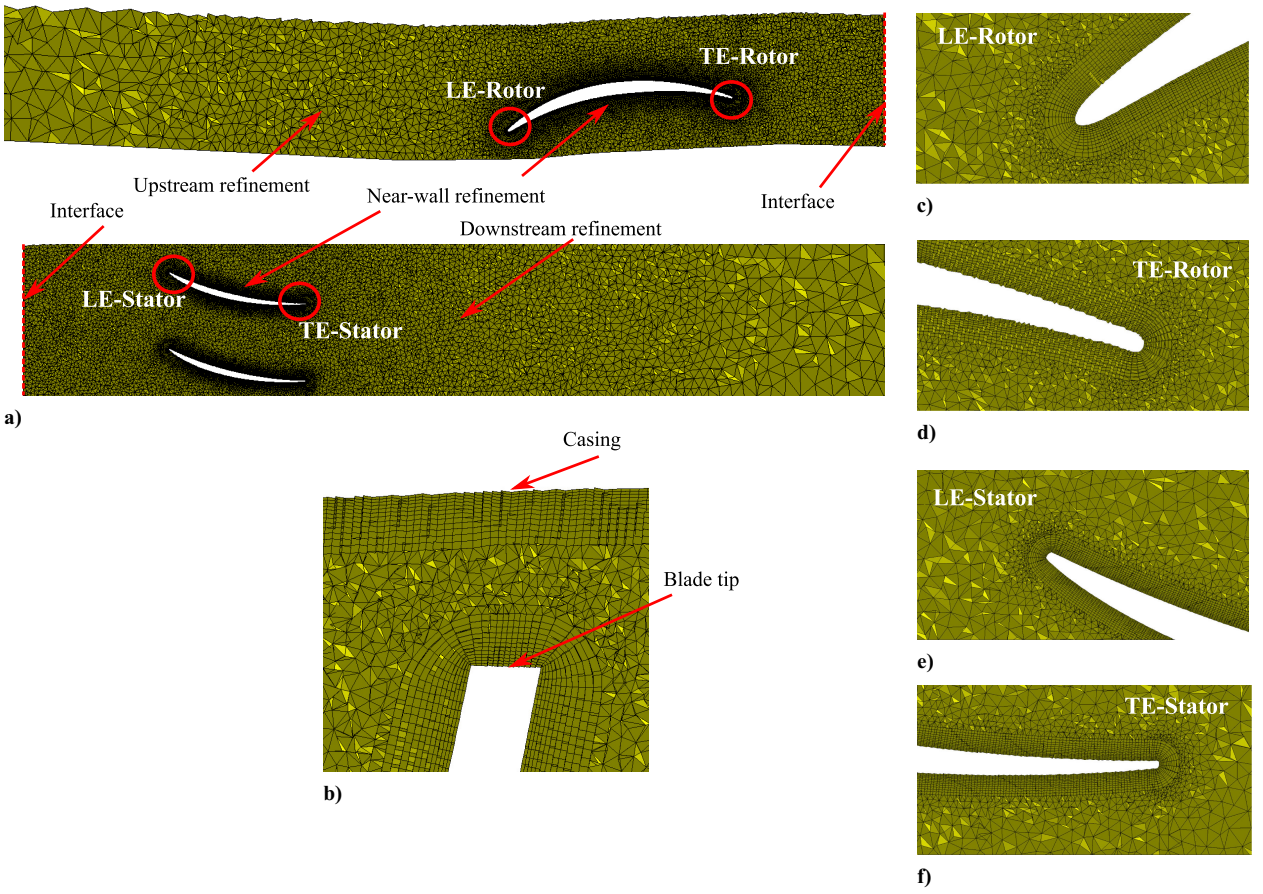

Fig. 2 a) Blade-to-blade mesh at midspan. Mesh refinement around the b) rotor tip, c) rotor leading edge, d) rotor trailing edge, e) stator leading edge, and f) stator trailing edge.

The mesh size and properties ensure a suitable resolution of turbulence in boundary layers and wakes, and the propagation of the acoustic waves in the fan stage without significant dissipation and dispersion errors.

The mesh properties for the periodic sector and 360-deg LES are shown in Table 2. The near-wall mesh refinement is based on predefined values of the dimensionless distances, which are given by Δx^+, Δy^+, and Δz^+ in the streamwise, wall-normal, and spanwise directions, respectively. These dimensionless wall distances are chosen according to recommended values for an accurate aeroacoustic LES of a fan stage [33]. The smallest cell size corresponds to the first prismatic layer on the wall surface. The cell size increases using an expansion ratio of 1.1.

Away from the walls, the mesh resolution is based on both turbulent and acoustic criteria [33]. At least 13 points per acoustic wavelength are used for frequencies up to 20 kHz. The acoustic wavelength can be calculated as $\lambda_{ac} = [c_0(1 - M)/f_c]$, where c_0 is the speed of sound, M is a mean Mach number, and $f_c = 20$ kHz is the target mesh cutoff frequency. This ensures a correct propagation of the acoustic waves below the target cutoff frequency of up to one fan chord length c_r, upstream of the rotor, and one OGV chord length c_s, downstream of the stator.

For a proper description of the turbulent structures in the wake region, the mesh size is smaller than 50 times the Taylor microscale, $\lambda_{Ta} = [10(\nu k_t/\epsilon)]^{(1/2)}$, where ν is the kinematic viscosity, k_t is the turbulent kinetic energy, and ϵ is the turbulent dissipation rate.

These criteria directly depend on the numerical scheme and mesh topology and have been found to provide accurate results in a previous work [33].

In the tip region, both prismatic and tetrahedral cells are used, and 30 points are imposed in the radial direction, as shown in Fig. 2b.

Table 2 Mesh properties of the LES grids. Δx^+, Δy^+, and Δz^+ are the maximum dimensionless wall distances in the streamwise, wall-normal, and spanwise directions, respectively

	Sector LES	360-deg LES
Number of cells [10^6]	95	1500
Δx^+ and Δz^+	150	150
Δy^+	25	25
Number of prism layers	10	10
expansion ratio	1.1	1.1
Time step [10^{-6} s/blade passage]	45.2	45.2
Sampling time [fan rotation]	4	4
CPUh/fan rotation [10^3]	105	1700

III. Temporal Convergence

Numerical and statistical convergences are studied here for both the periodic sector and the 360-deg LES. Numerical convergence corresponds to the end of the transient state, whereas statistical convergence corresponds to the convergence of the flow statistics. The convergence analysis methodology introduced by Boudet et al. [34] is adopted. Unsteady velocity data are collected for the convergence analysis. The monitor point used to collect the velocity samples is located in the suction-side boundary layer near the fan trailing edge, close to the blade-tip region, at a dimensionless wall-normal distance of $\Delta y^+ = 50$. The velocity samples are split into four segments and the statistical estimates on the last three segments are compared. The numerical convergence can be estimated by introducing the function

$$\kappa(u) = \max\left(\max_{i,j=2..4}\left(\left|\frac{\overline{u}^{(i)} - \overline{u}^{(j)}}{\overline{u}^{(4)}}\right|\right), \max_{i,j=2..4}\left(\left|\frac{u'^{(i)}_{\mathrm{RMS}} - u'^{(j)}_{\mathrm{RMS}}}{u'^{(4)}_{\mathrm{RMS}}}\right|\right)\right) \times 100 \quad (1)$$

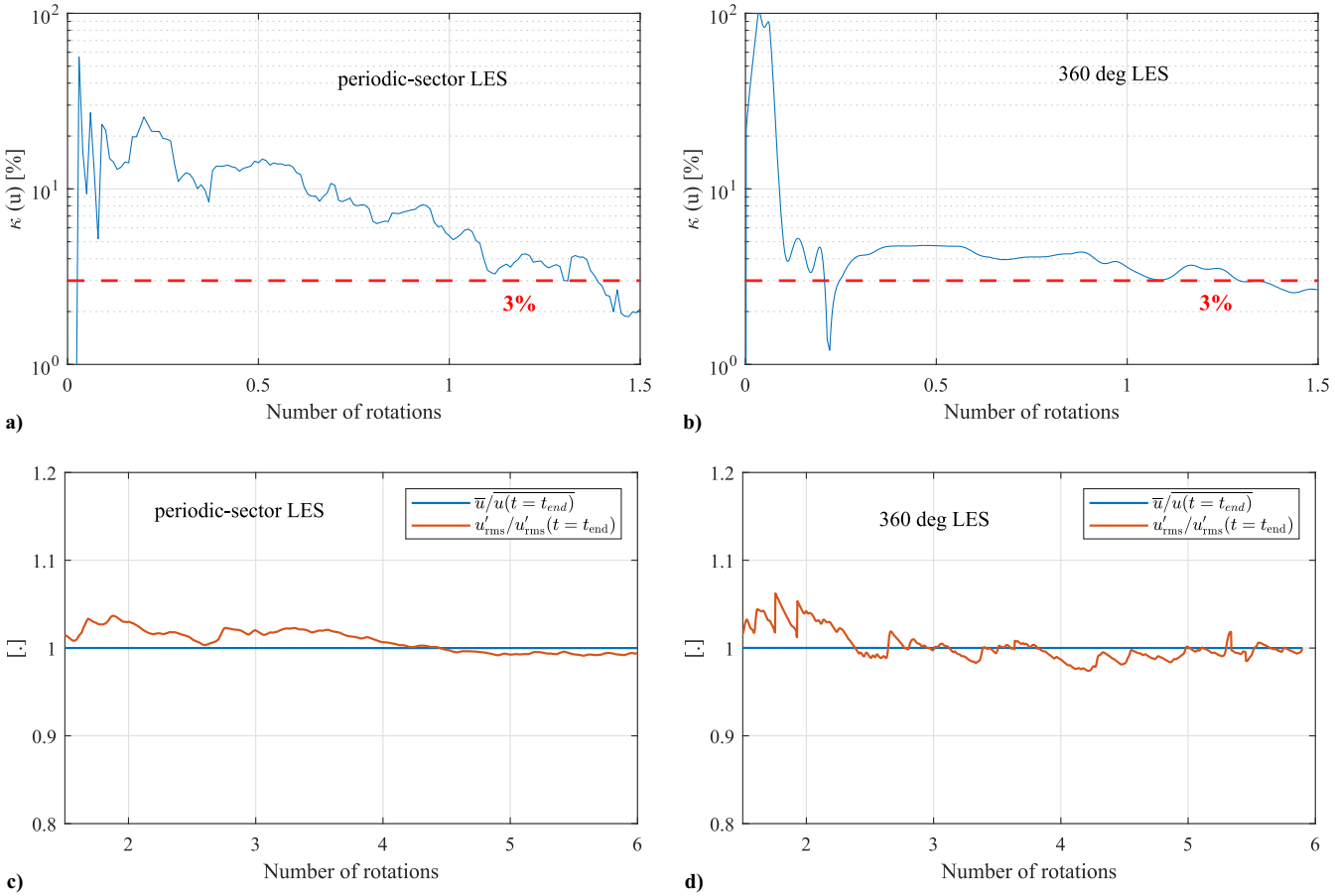

Fig. 3 Temporal convergence for the periodic sector and 360-deg LES. a/b) Numerical convergence over one segment of unsteady velocity samples, and c/d) statistical convergence. The average ($\bar{u}$) and the rms (u'_{rms}) of the streamwise velocity component are normalized by their values at the end of the simulation ($t = t_{\text{end}}$, where t corresponds to the time).

where $\overline{u}^{(i)}$ and $u'^{(i)}_{\text{RMS}}$ are the averaged velocity component and the root mean square (rms) velocity fluctuations, respectively, calculated over the ith segment.

The evolution of $\kappa(u)$ is presented in Figs. 3a and 3b over one segment. For both LES computations, numerical convergence is reached when variations in κ are approximately below 3%. Thus, the numerical convergence is reached at the end of the first segment.

The statistical convergence is considered to be satisfied when the statistics reach a constant value. Figure 3c shows the evolution of the average and the rms of the streamwise velocity component, both normalized by the values at the end of the simulation. It can be observed that the simulation is well converged after three full rotations. However, the simulations were continued to reach sufficient spectral resolution.

IV. Effects of Azimuthal Periodic Boundary Conditions

In this section, both the periodic sector and the 360-deg LES are assessed by comparing mean and turbulent parameters, as well as radial and azimuthal coherences. For the 360-deg LES, the parameters have been obtained from the circumferential average of all blade passages.

A. Instantaneous Flow Quantities

Figure 4 shows iso-contours of the Q-criterion ($Qc_r^2/U^2 = 10$, where U is the inflow velocity magnitude) for both the periodic sector and the 360-deg configurations. The iso-contours of the Q-criterion are colored by the vorticity magnitude. Turbulent structures of different sizes can be observed in the boundary layers and the wakes. Both configurations show a similar behavior. The transition of the boundary layers can be observed near the leading edges of the blades and vanes all along the span, which is consistent with LES results of other fan stages at approach conditions [12,35]. Small turbulent structures can be seen downstream of the transition regions. These turbulent structures are scattered by the trailing edges and generate trailing-edge noise. The turbulent structures in the rotor wake impinge on the leading edges of the stator vanes, which generate RSI noise. For both LES configurations, the iso-contours of the Q-criterion are presented along with contours of the instantaneous dilatation rate $\nabla \cdot \boldsymbol{u}$ at 99% of the rotor span. The wave fronts propagating in the upstream and downstream directions show the capability of both LES to compute the noise propagation in the refined-mesh region around the fan stage. It should be noted that spurious sound reflections cannot be seen from the upstream and downstream boundaries of the domain.

B. Mean Flow Quantities

Figure 5 shows a comparison of the isentropic Mach number distributions M_{is} from the periodic sector and the 360-deg LES, along the rotor and stator chord lengths at several spanwise locations. The isentropic Mach number, which is related to the static pressure distribution on the blade, is defined as

$$M_{is} = \sqrt{\left(\left(\frac{P_0}{P}\right)^{\gamma-1/\gamma} - 1\right)\frac{2}{\gamma - 1}} \tag{2}$$

where P_0 is the total pressure in the freestream outside the boundary layers, P is the static pressure, and $\gamma = 1.4$ corresponds to the ratio of specific heats.

On the rotor blade, similar results can be observed from both configurations at 50 and 80% of the rotor span (Figs. 5a and 5b). A small recirculation bubble is associated with a flat region close to the leading edge on the suction side at 80% of the rotor span, and seems to be captured by both simulations, as seen in Fig. 5b. The spanwise position at 98% of the rotor span, presented in Fig. 5c, is much closer to the tip-gap region and is affected by the tip-leakage flow. The isentropic

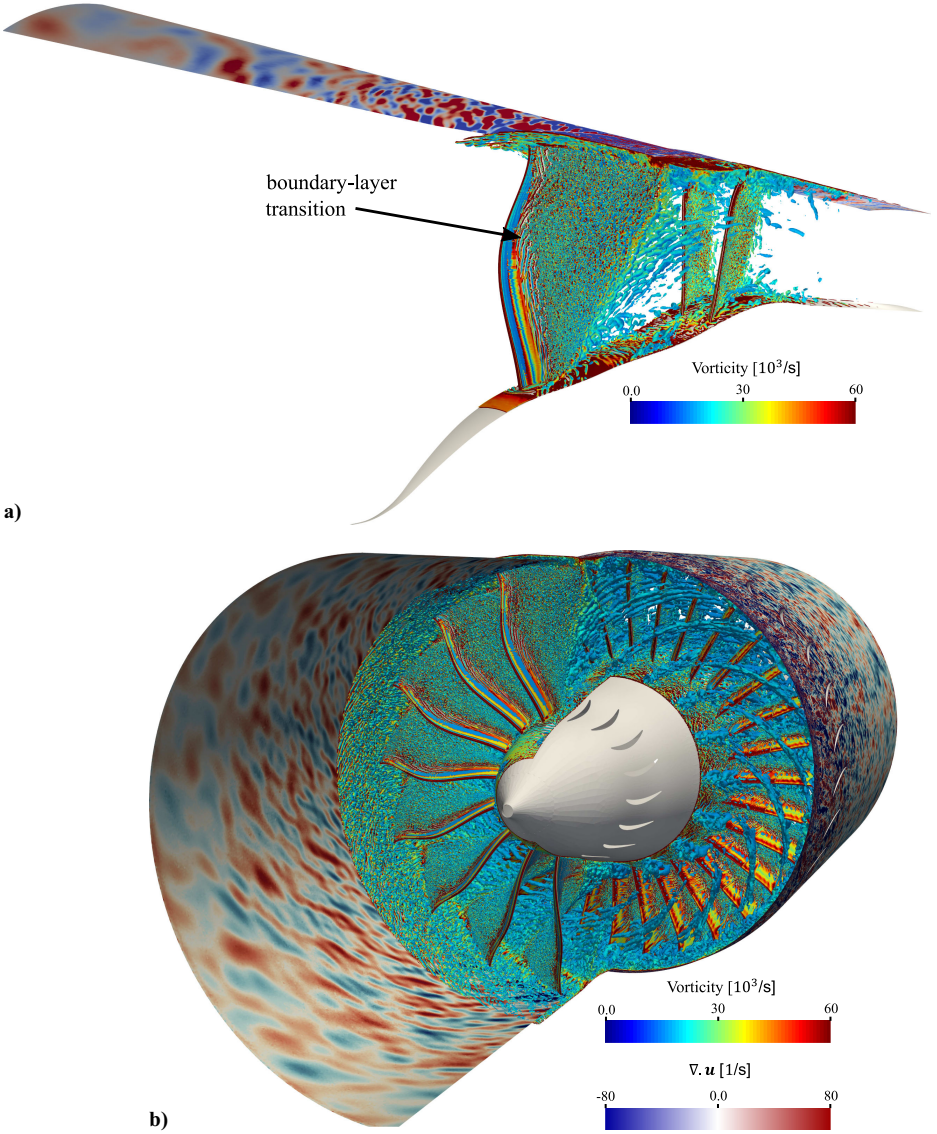

Fig. 4 Iso-contours of Q-criterion colored by vorticity magnitude in the fan stage and instantaneous contours of dilatation rate at 99% of the span. a) Periodic sector LES, and b) 360-deg LES.

Mach distribution between the leading edge and $0.4c_r$ is similar for both configurations. However, some differences can be observed between $0.6c_r$ and the trailing edge. For the periodic sector LES, a large pressure difference between the pressure and suction sides of the blade is observed in the vicinity of the trailing edge. This contrasts with the 360-deg LES, which presents a lower blade loading, and suggests that there might be some differences in the tip flow topology.

On the stator surface, Figs. 5d–5f show that the M_{is} distributions of the pressure and suction sides cross each other near the leading edge. This indicates that the stator is at negative angle of attack at approach condition, particularly near the shroud. However, slight differences can be observed between both simulations at different spanwise positions. These differences remain small and may be associated with the geometry modifications that have been introduced for the periodic sector LES, such as the chord reduction to maintain a constant solidity when changing the vane count from 31 to 32. Additionally, a small plateau in the M_{is} distribution can be observed in the 360-deg LES in Fig. 5f, on the pressure side between $0.05c_s$ and $0.1c_s$, which can be associated with a small recirculation bubble. This contrasts with the periodic-sector LES, in which the boundary-layer transition occurs at the leading edge.

The flow topology is then analyzed and compared in the fan-tip region between the periodic-sector and the 360-deg LES. Figure 6 shows the mean axial velocity component V_x and the turbulent kinetic energy k_t, which are averaged in the rotating reference frame. The tip- leakage flow of the ECL5 fan stage at approach condition has been extensively studied in a previous work by the authors [4]. For both the periodic-sector and 360-deg LES, an important axial velocity deficit develops between two consecutive blades near the trailing edge, as observed in region A in Fig. 6. The velocity deficit leads to a blockage effect. A strong increase in the axial velocity component, in region B in Fig. 6, appears close to the suction side from approximately $0.7c_r$ to the trailing edge. This corresponds to the region of large pressure difference between the pressure and suction sides of the blade in Fig. 5c and indicates the onset of a tip-leakage vortex. Large values of the axial velocity component can also be observed near the midchord of the fan blade, as shown in region C in Fig. 6. This highlights the presence of another tip-leakage vortex that is generated close to the leading edge of the fan-tip section. When comparing results from both configurations, the periodic-sector LES predicts larger V_x values on the suction side of the blade from $0.7c_r$ to the trailing edge, which is consistent with the larger blade loading observed in the M_{is} distribution in Fig. 5c.

The turbulent kinetic energy k_t is computed using the rms velocity fluctuations, $V_{x,\mathrm{rms}}$, $V_{\theta,\mathrm{rms}}$, and $V_{r,\mathrm{rms}}$ as

$$k_t = \frac{1}{\sqrt{2}}\sqrt{V_{x,\mathrm{rms}}^2 + V_{\theta,\mathrm{rms}}^2 + V_{r,\mathrm{rms}}^2} \tag{3}$$

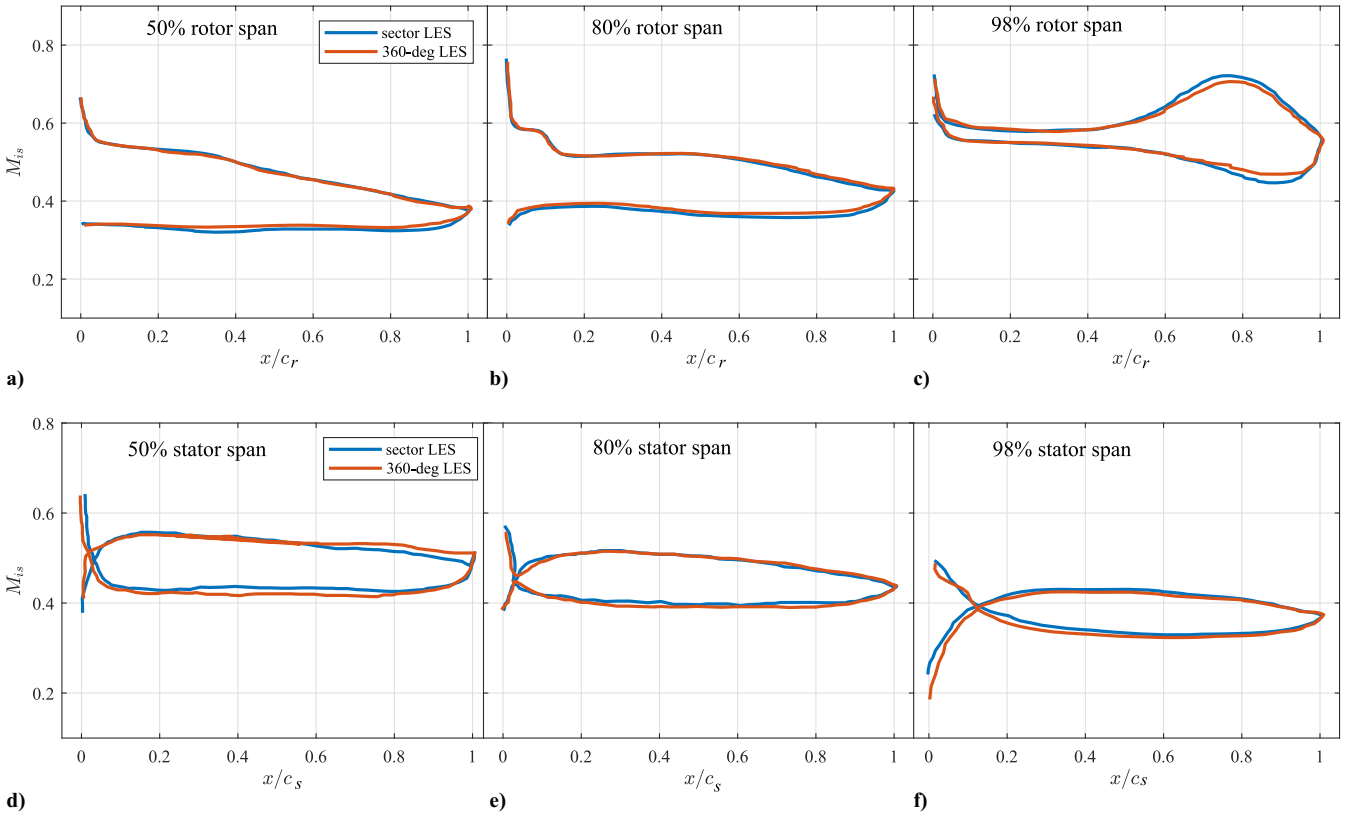

Fig. 5 Comparison of isentropic Mach-number distributions between the periodic sector and the 360-deg LES configurations.

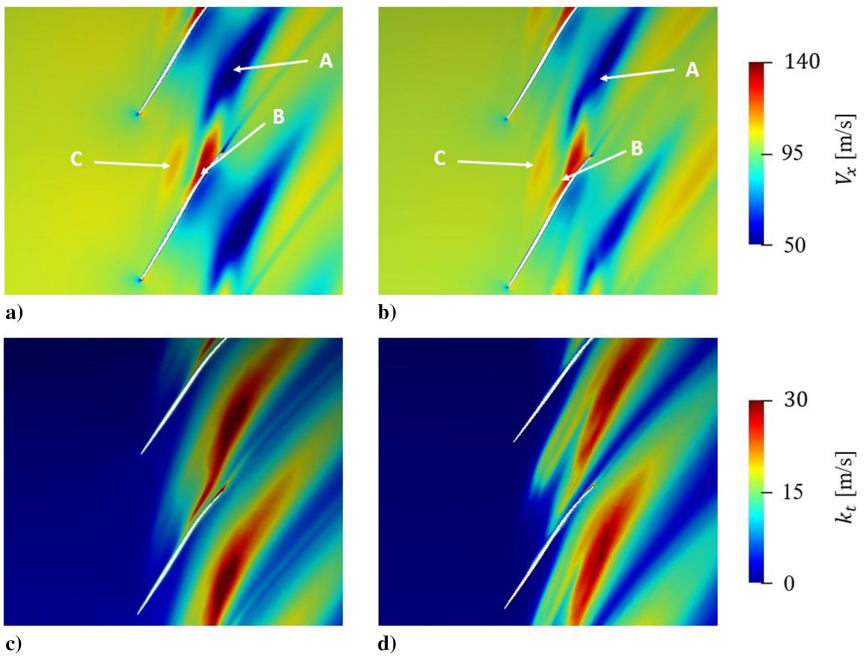

Fig. 6 Comparison of averaged axial velocity V_x and turbulent kinetic energy k_t at 98% of the fan span between the a/c) periodic-sector LES, and b/d) 360-deg LES.

Both the periodic sector and the 360-deg LES predict a region of high levels of k_t in the interblade region, particularly at the axial position of the trailing edge. This corresponds to the region of axial velocity deficit. The large turbulence levels can be associated with the velocity fluctuations generated by the interaction of different tip vortices with the main flow. The vortices generated from one blade interact with the trailing edge and the wake of the adjacent blade, as discussed in [4]. This interaction is more pronounced for the periodic-sector LES.

The radial distributions of the mean velocity components in the interstage, V_x, V_θ, and V_r, from the periodic-sector and 360-deg LES, are presented in Fig. 7. These time-averaged velocity profiles are calculated from the circumferential average of the velocity field at $0.5c_r$ downstream of the fan trailing edge. Both LES present similar results for the velocity components all along the span. A slight difference in V_r is observed from 60% to 90% of the fan span.

The radial distributions of the rms velocity fluctuations in the interstage, $V_{x,\mathrm{rms}}$, $V_{\theta,\mathrm{rms}}$, and $V_{r,\mathrm{rms}}$, from the periodic-sector and 360-deg

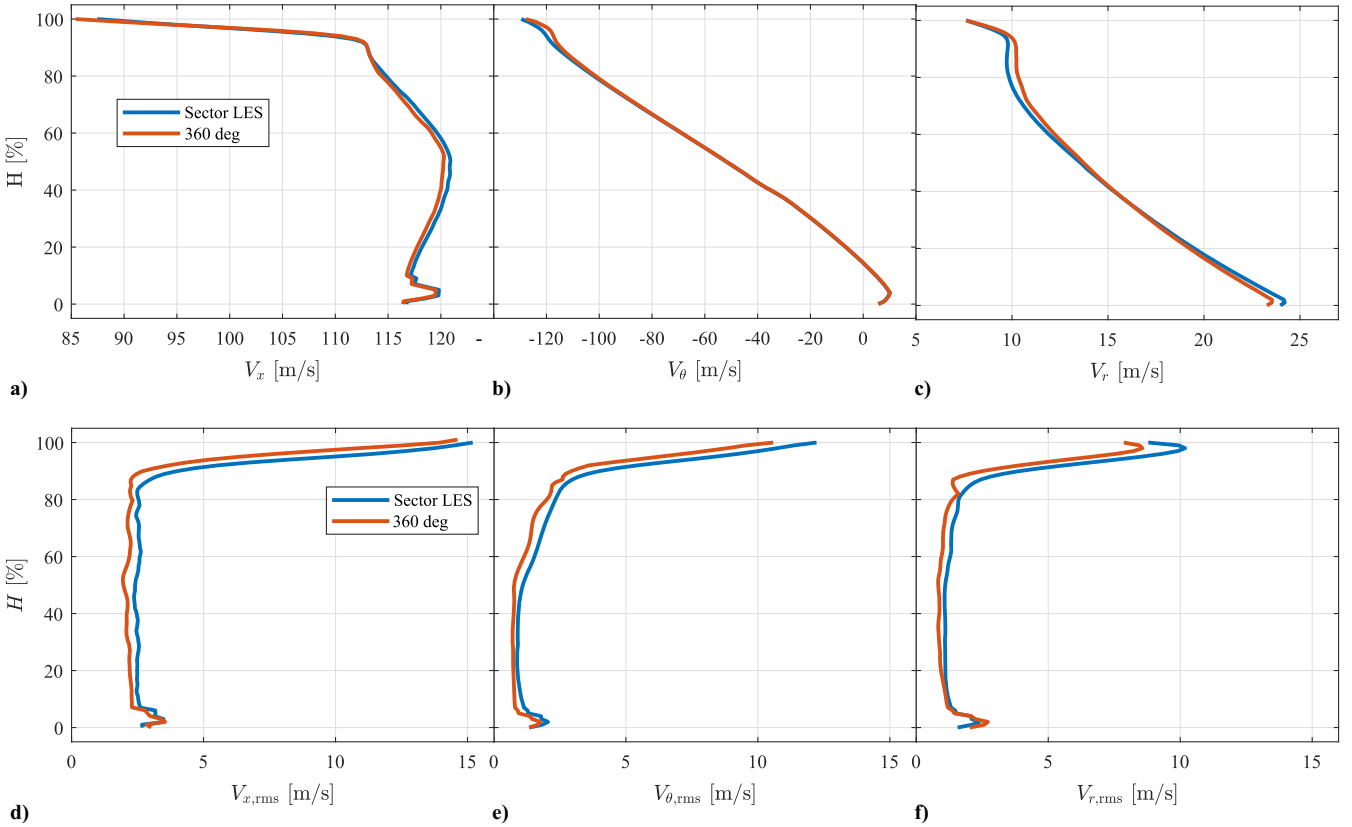

Fig. 7 Comparison of the radial distribution of a/b/c) mean, and d/e/f) rms velocity components, in the fan wake at $0.5c_r$ downstream of the fan trailing edge.

LES, are presented in Fig. 7. The rms of the velocity fluctuations are obtained from the circumferential average at $0.5c_r$ downstream of the fan trailing edge. Significant differences can be observed between the periodic-sector and the 360-deg configurations. The periodic sector predicts larger rms velocity fluctuations, particularly close to the blade tip, from 85% of the fan span to the outer casing. The fan-tip region shows a highly turbulent flow with several interactions between adjacent blades and in the interstage. Consequently, the main differences between both LES can be found in these regions. Moreover, the increase in $V_{\theta,\mathrm{rms}}$ from 50% to 85% of the span is more pronounced for the periodic-sector LES when compared with the 360-deg LES. It should be noted that there is a small flow-separation due to the apparition of a recirculation bubble in this region, as shown in Fig. 5b.

C. Coherence Analysis

A limitation of the periodic-sector LES is related to the perfect correlation between the fan passages in the circumferential direction. Conversely, the 360-deg LES can model the correlations without simplifying assumptions in the circumferential direction. The coherence function between the pressure fluctuations at two positions separated by a distance d_i in the ith direction can be written as

$$\gamma_i^2 = \frac{|S_{p_1p_2}(\omega)|^2}{S_{p_1p_1}(\omega)S_{p_2p_2}(\omega)} \tag{4}$$

where $S_{p_1p_2}$ is the cross-spectral density between the pressure fluctuations p_1 and p_2. $S_{p_1p_1}$ and $S_{p_2p_2}$ are the spectral densities of the pressure fluctuations p_1 and p_2, respectively.

Figure 8a presents a comparison of the coherence functions of the pressure fluctuations γ_θ^2 between the two positions $Pt\theta_1$ and $Pt\theta_2$ that are separated by approximately 360 deg $/(2B)$ in the circumferential direction. The coherence function was obtained at $0.5c_r$ downstream of the fan trailing edge. For the 360-deg LES, a piecewise circumferential averaging of the coherence is applied. At low and middle

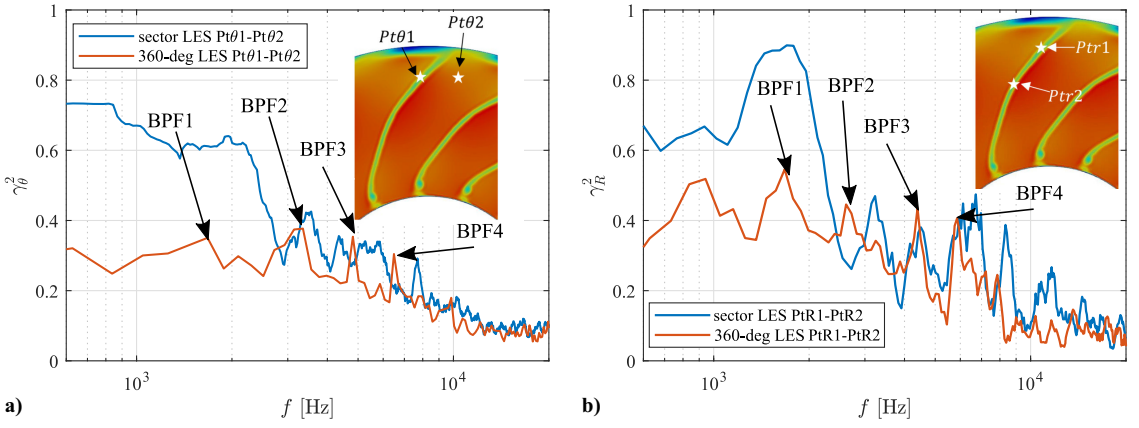

Fig. 8 Comparison of two-points coherence functions at different a) circumferential, and b) radial positions in the interstage, between the periodic sector and 360-deg LES.

frequencies, reduced coherence levels are obtained from the 360-deg LES configuration. These differences are related to the artificial correlation induced by the periodic condition in the sector LES, which has an effect on the large flow structures and low frequencies.

Figure 8b shows the coherence functions of the pressure fluctuations γ_R^2 between two positions $Ptr1$ and $Ptr2$ that are separated by approximately 10% of the fan diameter in the radial direction. For both configurations, spectral humps at the BPF (1613 Hz) and its harmonics are observed. For the 360-deg LES configuration, smaller coherence levels are obtained, particularly at low-to-middle frequencies (up to 2600 Hz), when compared with the periodic- sector LES. This is similar to the observations in Fig. 8a and can be explained by the suppression of the artificial correlation induced by the periodic boundary conditions in the circumferential direction and converted in the radial direction by the flow structures. At high frequencies, similar coherence levels are obtained for both configurations. This suggests that the periodic- sector LES may be sufficiently accurate for frequencies above the second harmonic of the bandpass filter (BPF, Blade Passing Frequency). However, fan noise from aeroengines often presents a maximum in both tonal and broadband noise between 0.5 and 3 times the BPF.

V. Noise Prediction

In the present section, the noise spectra from the fan stage are predicted directly from LES domains and compared to state-of-the-art analytical models. The RSI noise models used in this study are based on the work of Hanson [36] and Posson et al. [37,38]. These models are based on the model of Glegg [39], which analytically solves an integral equation of the sound field to obtain the cascade response using the Wiener–Hopf technique. These models for broadband noise account for the cascade effects and nonuniform flows in the spanwise direction by using a strip theory. Consequently, they allow for the consideration of complex flow properties and some features of the blade geometry, such as variable stagger, sweep, and lean angles. Additionally, duct propagation effects are included in the model of Posson et al. [37,38]. The trailing-edge-noise model adopted in this study is based on Amiet's theory [40,41], which describes the scattering of pressure fluctuations from a turbulent boundary layer at the trailing edge. The flow statistics from the fan stage are obtained from the periodic-sector LES and are used as input data to the analytical models. The validity of the input data has been assessed using empirical laws that are available in the literature. After the analysis of the spectra, the modal contents obtained from both the periodic-sector and 360-deg LES are also compared. For the 360-deg LES, the flow statistics have been obtained from the circumferential average of all blade passages.

A. Input data for RSI Noise Models

The turbulence spectrum of the axial velocity component $\Phi_{V_xV_x}$ can be used to characterize the RSI noise and is the main input parameter for RSI analytical noise models that assume isotropic turbulence [36–38]. $\Phi_{V_xV_x}$ can be directly extracted from the LES and can also be predicted by using a turbulence model, such as that of Liepmann and Von Karman. The objective of this section is to compare both LES turbulence velocity spectra to the isotropic turbulence model of Liepmann [42]. For both LES, $\Phi_{V_xV_x}$ is extracted at $0.03c_s$ upstream of the stator leading edge, which is sufficient to avoid a significant turbulence distortion near the stator [43,44]. To compute the Liepmann turbulence spectrum, the axial turbulence length scale λ has to be computed. λ is extracted from the periodic-sector LES in the present study to mimic common practices.

The axial turbulence length scale can be computed using different approaches, such as the frozen turbulence assumption, the empirical law of Jurdic et al. [45], and the limiting value of the power spectral density of the turbulence spectrum as the frequency approaches zero [46]. The first two approaches can be computed without using the turbulence spectrum from the LES and are further discussed as follows:

1) The first approach is based on Taylor's frozen turbulence assumption [45,47]. This implies that turbulent structures are convected unchanged by the mean flow over short distances. The unsteady velocity data, which are used to compute the autocorrelation function $R_{V_xV_x}$ are collected at $0.03c_s$ upstream of the OGV leading edge. $R_{V_xV_x}$ can be obtained from the LES as follows:

$$R_{V_xV_x}(\boldsymbol{x},\tau) = \frac{\overline{V_x'(\boldsymbol{x},t)V_x'(\boldsymbol{x},t+\tau)}}{V_{x,\mathrm{rms}}(\boldsymbol{x})^2} \tag{5}$$

where $V_x'(\boldsymbol{x},t)$ is the axial velocity fluctuation at position $\boldsymbol{x}$ and time t. The integral time scale λ_t can then be calculated as

$$\lambda_t = \int_{\tau=0}^{\infty} R_{V_xV_x}(\boldsymbol{x},\tau)\,\mathrm{d}\tau \tag{6}$$

and using Taylor's frozen turbulence assumption, the turbulence length scale λ_c can finally be computed as

$$\lambda_c = \overline{V_x}\lambda_t \tag{7}$$

where $\overline{V_x}$ is the circumferentially averaged axial velocity component at a distance of $0.03c_s$ upstream of the OGV leading edge.

2) The second approach is based on the semi-empirical law of Jurdic et al. [45] and requires the estimation of the wake width L_w from the numerical simulation. At each radial location, the wake width is computed from the circumferential distribution of turbulent kinetic energy. The turbulence length scale λ_j, in this case, is given as

$$\lambda_j = 0.21L_w \tag{8}$$

The radial distributions of the different turbulence length scale estimates λ_j and λ_c, obtained from the periodic-sector LES, are presented in Fig. 9a. The levels are consistent between both approaches. Overall, similar trends are observed between both λ_c and λ_j, which show an increase in the turbulence length scale near the hub and the casing. This is probably associated with the secondary flows in these regions, such as corner separation and tip-leakage vortices. The separation bubble in the tip region of the rotor may also play a role. It should be noted that both λ_c and λ_j present similar levels near the hub and the tip. This may not be expected, as λ_j is computed from the wake width, which is not correctly defined in the boundary layer near the hub and the fan-tip vortices near the outer casing.

In Fig. 9b, the turbulence velocity spectrum in the axial direction is extracted from both the periodic sector and 360-deg upstream of the stator leading edge at midspan and compared to the Liepmann model [42]. The input parameters for the Liepmann model, including the turbulence length scale and the turbulence intensity, are extracted from the periodic-sector LES. Model spectra using both λ_c and λ_j are compared, as the turbulence length scale can be difficult to predict accurately and may have a significant impact on fan broadband noise [15,48]. The peaks that appear in the turbulence spectra for both LES correspond to the BPF harmonics. The 360-deg LES predicts slightly smaller amplitudes at the BPF harmonics when compared to the periodic-sector LES. From 2 to 8 kHz, a good agreement can be found between both LES and the model of Liepmann informed by λ_c. At lower frequencies, i.e., below 2 kHz, the 360-deg LES shows lower levels than the periodic-sector LES, which are closer to the analytical predictions from the Liepmann model. In this frequency range, the differences in the model can be partly explained by the limited computational time in the simulations and the reduced size of the computational domain in the circumferential direction for the periodic-sector LES. At higher frequencies, i.e., above 8 kHz, both LES predict larger amplitudes than the Liepmann model. Overall, the Liepmann model informed by λ_j shows larger discrepancies with the LES results compared to the Liepmann model informed by λ_c, particularly at low and middle frequencies. Overall, the isotropic turbulence model of Liepmann, informed by a periodic-sector LES with λ_c, is sufficiently accurate for the prediction of the turbulence spectrum and RSI noise using analytical models. The anisotropy in the rotor wake, which may have an impact on the fan broadband noise [49], has not been included in this study.

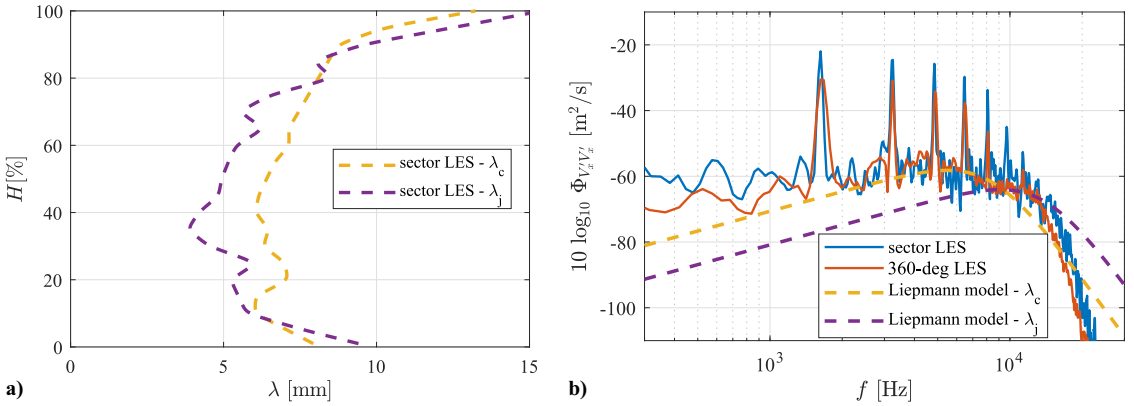

Fig. 9 a) Comparison of the turbulence length scales from the periodic-sector LES. The calculations are made upstream of the stator leading edge. b) Comparison of the turbulence spectrum of the axial velocity component at midspan between the periodic-sector LES, the 360-deg LES, and the turbulence model of Liepmann.

B. Input Data for Trailing-Edge-Noise Models

The trailing-edge noise is related to the flow properties in the boundary layers close to the trailing edge of the rotor blades and stator vanes. The two main parameters for the trailing- edge-noise analytical model [40,41] are (1) the wall-pressure spectrum Φ_{pp}, and (2) the spanwise correlation length l_z. These parameters can either be extracted from the LES or estimated using empirical models [50,51]. In the present study, the empirical models are informed by numerical data from the periodic-sector LES.

The wall-pressure spectra from both LES are compared with the empirical model of Rozenberg et al. [50], which is based on the model of Goody [52] and includes the effects of the Reynolds number and the adverse-pressure gradient. The required input data include internal parameters of the boundary layer, such as the wall shear stress, and external parameters, such as the convection velocity and the boundary-layer displacement thickness. These parameters are extracted from the periodic-sector LES on the suction side of the rotor blade and stator vane at $0.02c_r$ and $0.02c_s$ upstream of the trailing edge, respectively. The convection velocity corresponds to 70% of the velocity outside of the boundary layer. Figures 10a and 11a show the comparison of Φ_{pp} at midspan from LES and the empirical model of Rozenberg et al. [50]. Similar trends can be observed in the wall-pressure spectrum from LES and the empirical spectrum. However, lower levels in the amplitude of Φ_{pp} for the model can be observed, particularly for the stator.

The spanwise correlation lengths from both LES are compared with the empirical model of Salze et al. [51], which is based on the model of Efimtsov. [53] and has shown good results in a previous LES study [33]. In the direct LES approaches, l_z is estimated from the coherence function γ_z^2 between the pressure signals p_1 and p_2 at two points at the same axial position and separated by a spanwise distance Δz, as follows:

$$l_z(\omega) = \int_0^{+\infty} \sqrt{\gamma_z^2(\Delta z, \omega)}\, \mathrm{d}\Delta z \tag{9}$$

where the coherence function can be written as

$$\gamma_z^2 = \frac{|S_{p_1 p_2}(\omega)|^2}{S_{p_1 p_1}(\omega) S_{p_2 p_2}(\omega)} \tag{10}$$

The blades and vanes are divided into 20 radial strips in order to account for the radial variations in the boundary layer. Then, Amiet's trailing-edge-noise model [40,41] is applied to each strip. The contribution of each strip is summed incoherently. The value of l_z used for each strip is estimated using unsteady data collected from the LES and Eq. (9), which is calculated over the span of each strip. Figures 10b and 11b show the comparison of l_z at midspan from both LES and the model of Salze et al. [51].

When comparing the LES spectra Φ_{pp} to the empirical model of Rozenberg et al. [50], a good agreement is observed on the fan blade over the whole frequency range. l_z is underestimated by the model of Salze et al. [51], particularly on the stator vane. The empirical models only consider the diffraction of a turbulent boundary layer on a sharp trailing edge. However, other mechanisms generating disturbances in the boundary layers can be found in the LES, such as the impact of the rotor wakes on the stator vanes. This may explain the larger discrepancies between the LES results and the empirical models observed on the stator vanes. Furthermore, the coherence levels in the rotor wake from the periodic-sector and 360-deg LES show significant differences in Fig. 8, particularly at low frequencies. The rotor wakes impinge on the leading edges of the stator and may have an effect on the transition of the boundary layers on the stator vanes. This can partly explain the differences between the

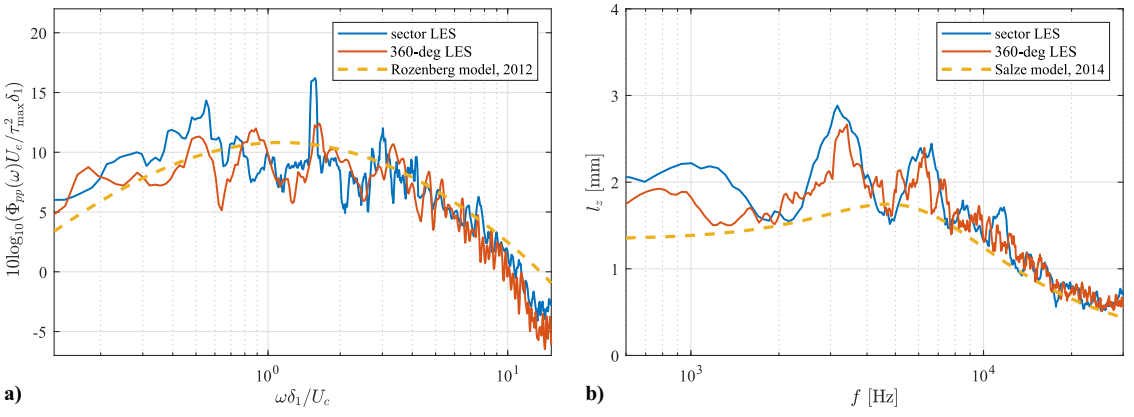

Fig. 10 Input parameters for Amiet's trailing-edge-noise model [40,41] on the suction side of the rotor blade at midspan. a) Wall-pressure spectrum, and b) spanwise correlation length.

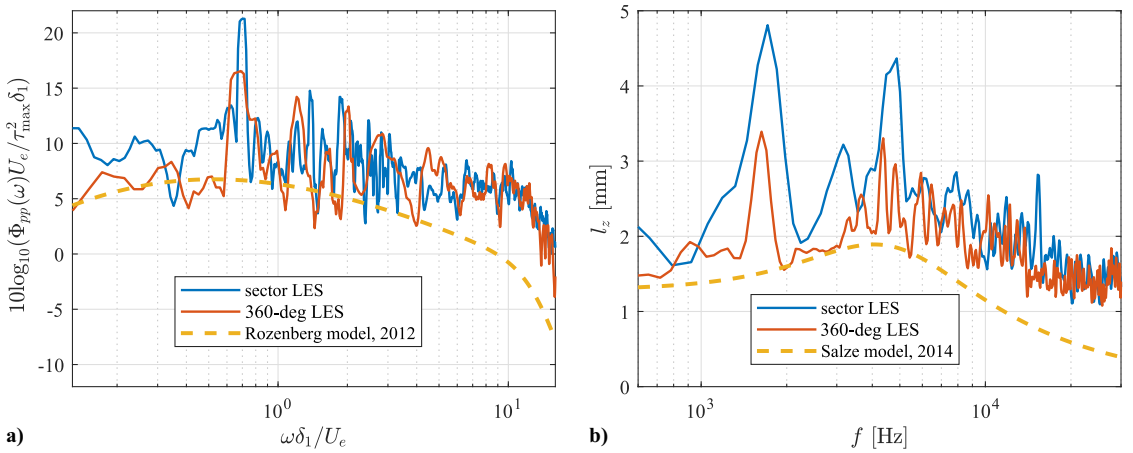

Fig. 11 Input parameters for Amiet's trailing-edge-noise model [40,41] on the suction side of the stator vane at midspan. a) Wall-pressure spectrum, and b) spanwise correlation length.

periodic sector and the 360-deg LES on the stator vanes, particularly at low and medium frequencies.

C. Sound Power Levels

The direct computations of the sound power levels from both the periodic-sector and the 360-deg LES are compared to the predictions from the analytical models. For the LES direct- noise predictions, the acoustic power W_a is computed by integrating the acoustic intensity I_a over a duct section and can be written as

$$W_a = \int_0^{2\pi} \int_{R_h}^{R_s} I_a r \, \mathrm{d}r \, \mathrm{d}\theta \tag{11}$$

where R_h and R_s are the hub and shroud radii, respectively. For a homentropic fluid, the acoustic intensity can be expressed as

$$I_a = \left(\frac{p'}{\rho_0} + U_0 V_x'^{\pm}\right)(\rho_0 V_x'^{\pm} + U_0 \rho'^{\pm}) \tag{12}$$

where p' refers to the pressure fluctuations, ρ_0 corresponds to the freestream density, $V_x'^{-}$ is the axial velocity fluctuations in the downstream direction, and $V_x'^{+}$ in the upstream direction. Monitor points for the direct LES noise predictions are located one rotor chord length upstream of the rotor blade and one stator chord length downstream of the stator vane. To properly capture the acoustic wave propagation, the mesh has been sufficiently refined in the region close to the rotor, stator, and monitor points. Furthermore, the axial location of the upstream extraction plane is near the spinner nose, where R_h is close to zero, and the axial location of the downstream extraction plane is in a region where R_s is nearly constant.

For the analytical modeling, the code *Optibrui* is used. The RSI noise is predicted using the analytical models of Hanson [36] and Posson et al. [37,38]. The trailing-edge noise from the rotor blades and stator vanes is predicted by Amiet's analytical model [40,41]. The contributions of both noise mechanisms are added incoherently. All the input parameters are extracted from the periodic-sector LES. For the RSI noise, the isotropic Liepmann turbulence model is informed by λ_c, as shown in Fig. 9b. For the trailing-edge noise, the input data are extracted at $0.98c_r$ and $0.98c_s$ from the leading edge on the suction side for each strip of the rotor blades and the stator vanes, respectively. It should be noted that the size of each radial strip is sufficiently larger than the integral length scale of the rotor wake turbulence and the spanwise correlation length from the boundary layer at the trailing edge, as required for the analytical models.

A comparison of the sound power levels (SWL) from the different approaches is shown in Fig. 12. The analytical models only include the broadband noise contribution, whereas both broadband and tonal noise are predicted by the LES computations. A fairly good agreement is obtained between the different approaches. Compared to the LES results, an underprediction of the sound power levels from the analytical models can be observed over the whole frequency range. This may be partially explained by additional noise sources that are present in the LES and are not modeled by the analytical models, such as the tip-gap noise. The tip-gap noise of the ECL5 at approach conditions has been studied in a previous work by the authors [4], and was found to contribute significantly to the

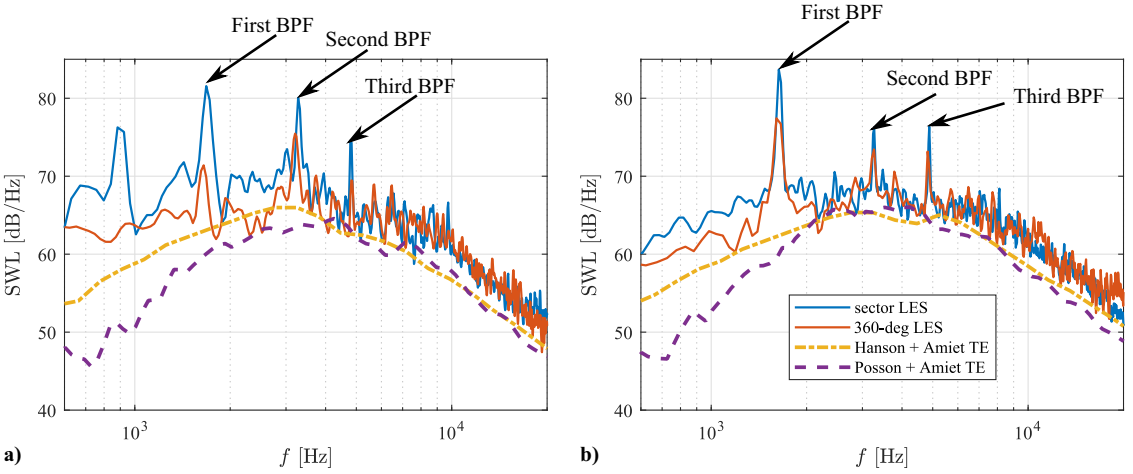

Fig. 12 Comparison between sound power levels between the periodic-sector LES and 360-deg LES predictions, in the a) upstream, and (b) downstream directions. The reference power level is 10^{-12} W.

SWL between 2 and 25 kHz in the upstream direction. When comparing both analytical models, noise predictions using the model of Posson et al. [37,38] are lower, particularly at low frequencies. This may be due to duct cutoff effects that are included in Posson et al.'s model [37,38] and are neglected in Hanson's model [36].

Lower SWL are obtained in the 360-deg LES when compared to the periodic-sector LES at low-to-middle frequencies, ranging from 600 to 5000 Hz in the upstream direction, and from 600 to 3000 Hz in the downstream direction. Differences of up to 5 dB in the broadband noise and 10 dB for the first BPF can be found in the upstream direction between both LES. The lower levels in the 360-deg configuration may be related to the reduced circumferential and radial coherence levels that were observed in Fig. 8, and to the smaller levels of the wall-pressure spectra and spanwise correlation lengths close to the trailing edge of the blades and vanes that were observed in Figs. 10 and 11. The reduced vane count used in the 360-deg LES when compared to the periodic-sector LES can also lead to a slight broadband noise increase in the periodic-sector LES.

D. Modal Content

One of the main advantages of the 360-deg LES is the ability to obtain a complete modal content from the circumferential decomposition of the acoustic field radiated by the fan stage. Assuming acoustic propagation in an annular duct with rigid walls and a constant Mach number flow, the acoustic pressure $p'(r,\theta,x,t)$ can be obtained from the convected Helmholtz equation and can be written as a weighted summation of modes [54]:

$$p'(r,\theta,x,t) = \sum_{m=-\infty}^{\infty}\sum_{j=0}^{\infty}\left(A_{mj}^{+}e^{ik_{mj}^{+}x} + A_{mj}^{-}e^{ik_{mj}^{-}x}\right)f_{mj}(r)e^{im\theta}e^{-i\omega t} \tag{13}$$

where ω is the angular frequency, and A_{mj}^{+} and A_{mj}^{-} are the modal amplitudes of the waves propagating downstream and upstream, respectively. The subscripts m and j represent the circumferential and radial modal orders, $k_{mj}^{\pm}$ are the axial wavenumbers in the downstream (+) and upstream (−) directions, and $f_{mj}(r)$ is a normalized modal radial function, which includes the Bessels functions of the first and second kind. The function $f_{mj}(r)$ only depends on the cross-section of the annular duct and radial boundary conditions. For further details on the wave numbers and the modal radial functions, the reader is referred to Ref. [54].

For both LES configurations, the modal content is computed using a polar mesh of 200 monitor points in the circumferential direction and 20 monitor points in the radial direction, which are located on the extraction planes upstream of the fan and downstream of the OGV, as discussed in Sec. V.C. The circumferential modal content corresponding the first radial mode for the first, second, third, and fourth BPF harmonics is presented in Figs. 13 and 14 in the upstream and downstream directions, respectively. For each BPF harmonic, the limit of the cut-on mode threshold for the first radial mode is presented by the black dashed lines, given by $K_{m,j}$, which represents the eigenvalue of the duct mode (m, j) as

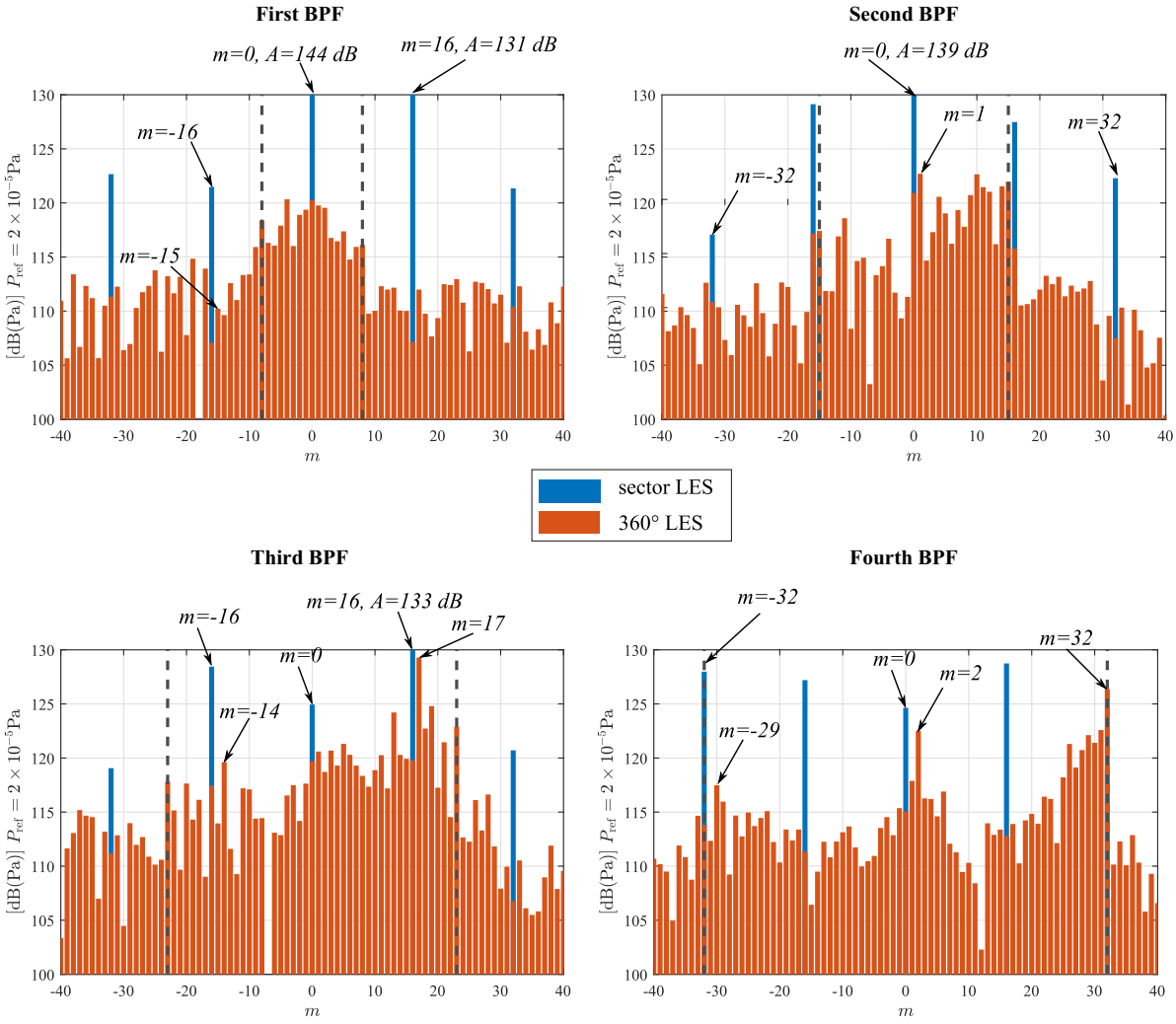

Fig. 13 Comparison between the periodic sector and the 360-deg LES of the circumferential mode distribution in the upstream direction for different BPF harmonics. The dashed lines indicate the limit of the cut-on mode threshold. "*A*" refers to the modal amplitude.

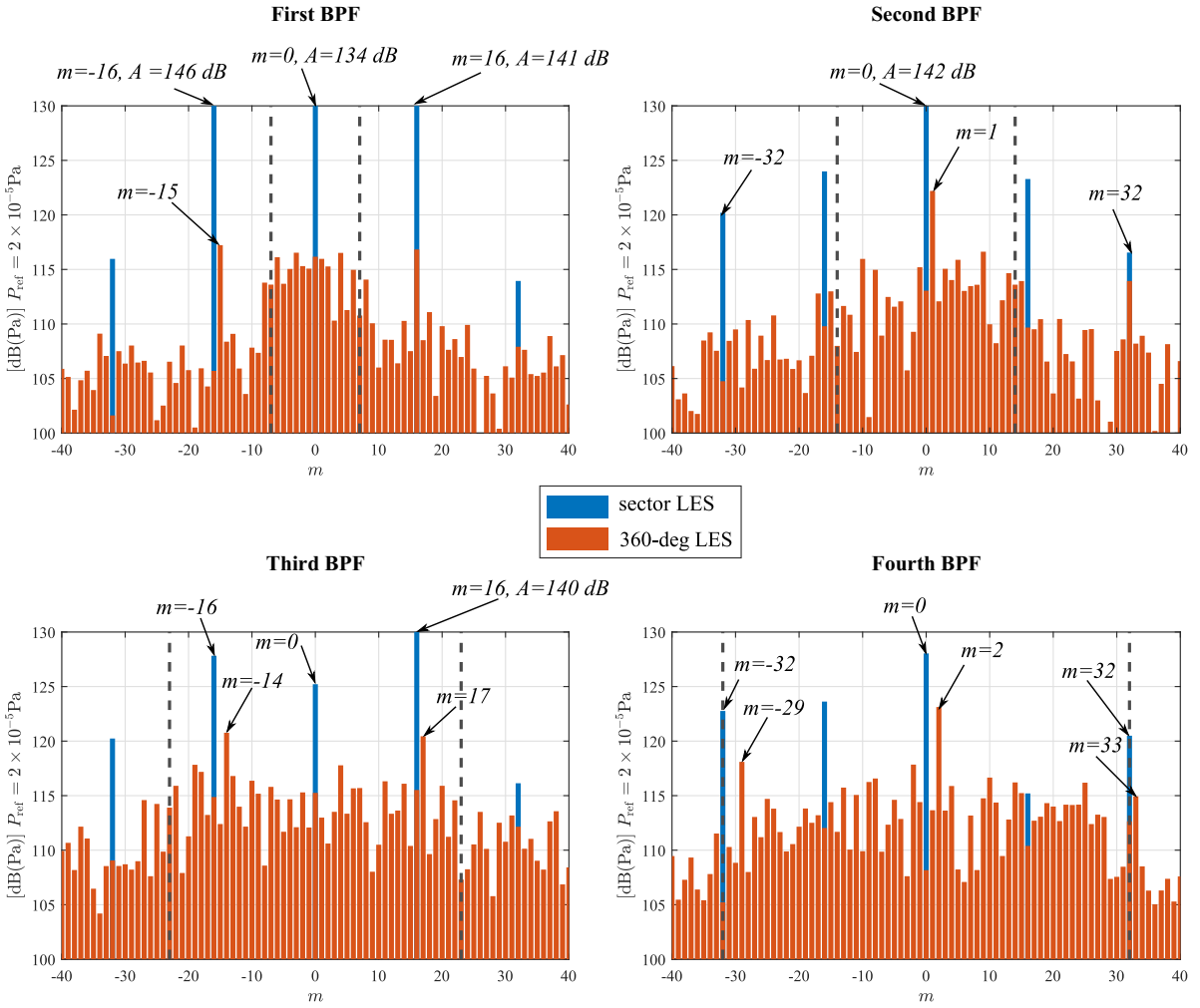

Fig. 14 Comparison between the periodic sector and the 360-deg LES of the circumferential mode distribution in the downstream direction for different BPF harmonics. The dashed lines indicate the limit of the cut-on mode threshold. "*A*" refers to the modal amplitude.

$$K_{m,j} = \frac{2\pi f}{c_0 \beta} \tag{14}$$

where $\beta = \sqrt{1 - M^2}$ is the compressibility parameter. Once $K_{m,j}$ is computed, the circumferential order of the cut-on zone can be obtained for each radial order, as detailed in [54].

Based on the Tyler and Sofrin rule [55], the acoustic modes associated with the tonal interaction noise at the BPF and its harmonics have circumferential orders $m = nB - sV$, where n is the BPF order and s is an integer. In this case, $B = 16$ for both configurations, whereas $V = 32$ for the periodic-sector LES and $V = 31$ for the 360-deg LES. The Tyler and Sofrin modes for both configurations are given in Table 3.

Cutoff modes are well attenuated as expected from the Tyler and Sofrin rule, except for the first BPF. It should be noted that for the first BPF, the cut-on circumferential modes cannot be explained by a Tyler and Sofrin rule, which only includes the interaction modes. Furthermore, there is a significant contribution of the broadband noise to the cut-on circumferential modes, which is mainly related to the interaction of the turbulent wakes with the leading edges of the stator. Consequently, the broadband noise contributes to the amplitude of the mode of order $m = 0$ for the periodic-sector LES, and some cut-on modes for the 360-deg LES. Additionally, the presence of these modes can be partly related to a modal scattering mechanism, which is associated with some reflections on the stator vanes and the rotor blades. Furthermore, the reduced time used for the data recording, compared to the recording time usually used in experimental campaigns for modal content analyses, may also explain some of the additional modes, such as the acoustic modes of circumferential order $m = -16$ and $m = 16$ for the periodic-sector LES, and $m = -15$ and $m = 16$ for the 360-deg LES. Moreover, the downstream extraction plane, which is located at c_s from the stator trailing edges, may also be relatively close to the stator vanes such that some of the cut-off modes may not have sufficiently decayed. Additionally, hydrodynamics fluctuations due to the wakes can also impact some of the modes at the downstream location. These modes remain limited and their amplitudes are much smaller than the cut-on modes. For the other BPF harmonics, additional Tyler and Sofrin modes become cut-on.

Table 3 Tyler and Sofrin modes for different BPF harmonics

	n	s	m (Periodic-sector LES)	m (360-deg LES)
First BPF	1	0	16	16
		1	−16	−15
Second BPF	2	0	32	32
		1	0	1
		2	−32	−30
Third BPF	3	1	16	17
		2	−16	−14
Fourth BPF	4	1	32	33
		2	0	2
		3	−32	−29

Significant differences in the acoustic content can be observed when comparing the results from the periodic sector and the 360-deg LES. Only the circumferential modal orders $m = 0$ and the multiples of $m = \pm 16$ can exist in the periodic-sector LES, whereas all the acoustic modes can be produced when the complete azimuthal extent is considered. This directly highlights the limitations of a periodic-sector LES to study and improve current understanding of

the acoustic field in the fan stage. For the first and second BPF harmonics, the Tyler and Sofrin modes show significantly larger modal amplitudes in the periodic-sector LES when compared to the 360-deg LES. This may explain the larger SWL observed at these frequencies in the upstream and downstream directions, as shown in Fig. 12.

VI. Conclusions

In the present study, the influence of the periodic azimuthal boundary conditions on the flow topology and noise emissions of a fan stage has been investigated. To this end, the ECL5 fan stage designed at Ecole Centrale de Lyon, which is representative of a modern ultrahigh- bypass-ratio fan stage, has been studied at approach condition. A full 360-deg LES has been performed with a high resolution to improve current understanding of fan noise and has been compared to a periodic-sector LES. The noise has been directly computed from the LES using a well-refined mesh.

The pressure distribution along the rotor blades and stator vanes, as well as the mean velocity components in the interstage region, show similar results for both configurations. Some differences are found for the rms velocity fluctuations in the rotor wake region, with lower values in the 360-deg large-eddy simulation (LES). The 360-deg LES also predicts lower coherence levels, particularly in the low- and middle-frequency range, due to the spurious correlation induced between the azimuthal boundaries by the periodic condition in the sector LES. These periodic boundary conditions mainly affect the large scales and thus the low frequencies. Consequently, the periodic-sector LES predicts larger sound-power levels upstream and downstream of the fan stage, particularly at low-to-middle frequencies. Analytical models for the rotor–stator-interaction noise and trailing-edge noise have also been used to predict the noise spectra. These models tend to underestimate the noise compared to the LES results over the whole range of frequencies. This can mainly be explained by the presence of additional noise sources in the LES that are not reproduced by these analytical models, such as the tip-leakage noise. Additionally, the assumptions used for the analytical models, such as a turbulence isotropy model and a frozen gust assumption, may also partially explain this difference.

The modal content of the ECL5 fan stage noise has also been computed from the periodic-sector and the 360-deg LES. For both configurations, a radial and azimuthal modal decomposition has been performed. The cutoff modes seem to be sufficiently attenuated, except for the first BPF. For different harmonics of the BPF, the Tyler and Sofrin modes were clearly identified in the modal content in the upstream and downstream directions. For the periodic sector, the modal decomposition is limited by the circumferential extent of computational domain, whereas a complete circumferential decomposition can be obtained for the 360-deg LES. The acoustic modes generated by the fan stage are thus directly influenced by the circumferential extent of the periodic sector and are significantly different from those of the 360-deg LES. Consequently, the periodic-sector LES cannot reproduce the correct modal content of the fan stage. This constitutes an important limitation of the numerical simulations using periodic boundary conditions, which cannot properly compute the acoustic field from turbofan engines.

Acknowledgments

This work was performed within the framework of the industrial chair ARENA (ANR-18-CHIN-0004-01) cofinanced by Safran Aircraft Engines and the French National Research Agency (ANR), and is also supported by the Labex CeLyA of the Université de Lyon, operated by the French National Research Agency (ANR-11-LABX-0060/ANR-16-IDEX-0005). The computational resources were provided by a PRACE European award (project LESFAN, proposal no. 2021240101), GENCI (CINES, project number A0082A05 039), and by FLMSN-PMCS2I at Ecole Centrale de Lyon. The authors would like to thank Safran, Airbus, and Valeo for providing access to the Optibrui software. The authors also acknowledge Michel Roger, Stéphane Aubert, Christoph Brandstetter, Xavier Ottavy, Pascal Ferrand, Danny Lewis, and Valdo Pagès from the Laboratoire de Mécanique des Fluides et d'Acoustique of Ecole Centrale de Lyon and Hélène de Laborderie from Safran Aircraft Engines for their precious advice. Most of the postprocessing was performed using Antares (release 1.16.0).

References

[1] Moreau, S., "Turbomachinery Noise Predictions: Present and Future," *Acoustics*, Vol. 1, No. 1, 2019, pp. 92–116. https://doi.org/10.3390/acoustics1010008

[2] Liu, X., Zhao, D., Guan, D., Becker, S., Sun, D., and Sun, X., "Development and Progress in Aeroacoustic Noise Reduction on Turbofan Aeroengines," *Progress in Aerospace Sciences*, Vol. 130, April 2022, Paper 100796. https://doi.org/10.1016/j.paerosci.2021.100796

[3] Tyler, J., and Sofrin, T., "Axial Flow Compressor Noise Studies," *Society of Automotive Engineers Transactions*, Vol. 70, 1962, pp. 309–332. https://doi.org/10.4271/620532

[4] Al Am, J., Clair, V., Giauque, A., Boudet, J., and Gea-Aguilera, F., "Aeroacoustic Analysis of the Tip-Leakage Flow of an Ultra High Bypass Ratio Fan Stage," *Physics of Fluids*, Vol. 35, No. 4, 2023, Paper 047104. https://doi.org/10.1063/5.0146143

[5] Roger, M., and Moreau, S., "Back-Scattering Correction and Further Extensions of Amiet's Trailing-Edge Noise Model. Part 1: Theory," *Journal of Sound and Vibration*, Vol. 286, No. 3, 2005, pp. 477–506. https://doi.org/10.1016/j.jsv.2004.10.054

[6] Al-Am, J., Clair, V., Giauque, A., Boudet, J., and Gea-Aguilera, F., "On the Effects of a Separation Bubble on Fan Noise," *Journal of Sound and Vibration*, Vol. 537, Oct. 2022, Paper 117180. https://doi.org/10.1016/j.jsv.2022.117180

[7] Amiet, R. K., "Acoustic Radiation from an Airfoil in a Turbulent Stream," *Journal of Sound and Vibration*, Vol. 41, No. 4, 1975, pp. 407–420. https://doi.org/10.1016/S0022-460X(75)80105-2

[8] Peake, N., and Parry, A. B., "Modern Challenges Facing Turbomachinery Aeroacoustics," *Annual Review of Fluid Mechanics*, Vol. 44, Jan. 2012, pp. 227–248. https://doi.org/10.1146/annurev-fluid-120710-101231

[9] Lewis, D., de Laborderie, J., Sanjosé, M., Moreau, S., Jacob, M. C., and Masson, V., "Parametric Study on State-of-the-Art Analytical Models for Fan Broadband Interaction Noise Predictions," *Journal of Sound and Vibration*, Vol. 514, Dec. 2021, Paper 116423. https://doi.org/10.1016/j.jsv.2021.116423

[10] Moreau, S., and Roger, M., "Advanced Noise Modeling for Future Propulsion Systems," *International Journal of Aeroacoustics*, Vol. 17, Nos. 6–8, 2018, pp. 576–599. https://doi.org/10.1177/1475472X18789005

[11] Pérez Arroyo, C., Leonard, T., Sanjosé, M., Moreau, S., and Duchaine, F., "Large Eddy Simulation of a Scale-Model Turbofan for Fan Noise Source Diagnostic," *Journal of Sound and Vibration*, Vol. 445, April 2019, pp. 64–76. https://doi.org/10.1016/j.jsv.2019.01.005

[12] Lewis, D., Moreau, S., Jacob, M. C., and Sanjosé, M., "ACAT1 Fan Stage Broadband Noise Prediction Using Large-Eddy Simulation and Analytical Models," *AIAA Journal*, Vol. 60, No. 1, 2022, pp. 360–380. https://doi.org/10.2514/1.J060163

[13] Al Am, J., Clair, V., Giauque, A., Boudet, J., and Gea-Aguilera, F., "Direct Noise Predictions of Fan Broadband Noise Using LES and Analytical Models," *28th AIAA/CEAS Aeroacoustics Conference*, AIAA Paper 2022-2882, 2022. https://doi.org/10.2514/6.2022-2882

[14] Grace, S., Gonzalez-Martino, I., and Casalino, D., "Analysis of Fan-Stage Gap-Flow Data to Inform Simulation of Fan Broadband Noise," *Philosophical Transactions of the Royal Society A*, Vol. 377, No. 2159, 2019, Paper 20190080. https://doi.org/10.1098/rsta.2019.0080

[15] Kissner, C., Guérin, S., Seeler, P., Billson, M., Chaitanya, P., Carrasco Laraña, P., de Laborderie, H., François, B., Lefarth, K., Lewis, D., et al., "ACAT1 Benchmark of RANS-Informed Analytical Methods for Fan Broadband Noise Prediction—Part I—Influence of the RANS Simulation," *Acoustics*, Vol. 2, No. 3, 2020, pp. 539–578. https://doi.org/10.3390/acoustics2030029

[16] Casalino, D., Hazir, A., and Mann, A., "Turbofan Broadband Noise Prediction Using the Lattice Boltzmann Method," *AIAA Journal*, Vol. 56, No. 2, 2018, pp. 609–628. https://doi.org/10.2514/1.J055674

[17] Williams, J. F., and Hawkings, D. L., "Sound Generation by Turbulence and Surfaces in Arbitrary Motion," *Philosophical Transactions for the Royal Society of London. Series A, Mathematical and Physical Sciences*, Vol. 254, No. 1151, 1969, pp. 321–342. https://doi.org/10.1098/rsta.1969.0031

[18] Goldstein, M., *Aeroacoustics*, Advanced Book Program, McGraw-Hill International Book Company, New York, 1976, https://books.google.com.lb/books?id=HY1TAAAAMAAJ.

[19] Régis, K., Marlène, S., and Stéphane, M., "Aerodynamic Investigation of a Linear Cascade with Tip Gap Using Large-Eddy Simulation," *Journal of the Global Power and Propulsion Society*, Vol. 5, April 2021, pp. 39–49. https://doi.org/10.33737/jgpps/133601

[20] Pereira, A., and Jacob, M. C., "Modal Analysis of In-Duct Fan Broadband Noise via an Iterative Bayesian Inverse Approach," *Journal of Sound and Vibration*, Vol. 520, March 2022, Paper 116633. https://doi.org/10.1016/j.jsv.2021.116633

[21] Rai, M. M., and Madavan, N. K., "Multi-Airfoil Navier–Stokes Simulations of Turbine Rotor–Stator Interaction," *Journal of Turbomachinery*, Vol. 112, No. 3, 1990, pp. 377–384. https://doi.org/10.1115/1.2927670

[22] Pagès, V., Duquesne, P., Aubert, S., Blanc, L., Ferrand, P., Ottavy, X., and Brandstetter, C., "UHBR Open-Test-Case Fan ECL5/CATANA," *International Journal of Turbomachinery, Propulsion and Power*, Vol. 7, No. 2, 2022, p. 17. https://doi.org/10.3390/ijtpp7020017

[23] Brandstetter, C., Pagès, V., Duquesne, P., Ottavy, X., Ferrand, P., Aubert, S., and Blanc, L., "UHBR Open-Test-Case Fan ECL5/CATANA Part 1: Geometry and Aerodynamic Performance," *14th European Conference on Turbomachinery Fluid Dynamics & Thermodynamics*, NB 626, EuroTurbo European Turbomachine Soc., 2021.

[24] Pagès, V., Duquesne, P., Aubert, S., Blanc, L., Ferrand, P., Ottavy, X., and Brandstetter, C., "UHBR Open-Test-Case Fan ECL5/CATANA, Part 2: Mechanical and Aeroelastic Stability Analysis," *14th European Conference on Turbomachinery Fluid Dynamics & Thermodynamics*, NB 625, EuroTurbo European Turbomachine Soc., 2021.

[25] Fiquet, A.-L., Ottavy, X., and Brandstetter, C., "UHBR Open-Test Case Fan ECL5/CATANA: Non-Linear Analysis of Non-Synchronous Blade Vibration at Part-Speed Conditions," *16th International Symposium on Unsteady Aerodynamics Aeroacoustics and Aeroelasticity of Turbomachine*, ISUAAAT-16, HAL, France, Sept. 2022.

[26] Fiquet, A.-L., Schneider, A. P., Paoletti, B., Ottavy, X., and Brandstetter, C., "Experiments on Tuned UHBR Open-Test Case Fan ECL5/CATANA: Stability Limit," *ASME Turbo Expo*, American Soc. of Mechanical Engineers, Fairfield, NJ, June 2023, Paper V11AT21A009.

[27] Schonfeld, T., and Rudgyard, M., "Steady and Unsteady Flow Simulations Using the Hybrid Flow Solver AVBP," *AIAA Journal*, Vol. 37, No. 11, 1999, pp. 1378–1385. https://doi.org/10.2514/2.636

[28] Wang, G., Duchaine, F., Papadogiannis, D., Duran, I., Moreau, S., and Gicquel, L. Y., "An Overset Grid Method for Large Eddy Simulation of Turbomachinery Stages," *Journal of Computational Physics*, Vol. 274, Oct. 2014, pp. 333–355. https://doi.org/10.1016/j.jcp.2014.06.006

[29] Colin, O., and Rudgyard, M., "Development of High-Order Taylor-Galerkin Schemes for LES," *Journal of Computational Physics*, Vol. 162, No. 2, 2000, pp. 338–371. https://doi.org/10.1006/jcph.2000.6538

[30] Nicoud, F., Toda, H. B., Cabrit, O., Bose, S., and Lee, J., "Using Singular Values to Build a Subgrid-Scale Model for Large Eddy Simulations," *Physics of Fluids*, Vol. 23, No. 8, 2011, Paper 085106. https://doi.org/10.1063/1.3623274

[31] Poinsot, T., and Lele, S., "Boundary Conditions for Direct Simulations of Compressible Viscous Flows," *Journal of Computational Physics*, Vol. 101, No. 1, 1992, pp. 104–129. https://doi.org/10.1016/0021-9991(92)90046-2

[32] Schmitt, P., Poinsot, T., Schuermans, B., and Geigle, K. P., "Large-Eddy Simulation and Experimental Study of Heat Transfer, Nitric Oxide Emissions and Combustion Instability in a Swirled Turbulent High-Pressure Burner," *Journal of Fluid Mechanics*, Vol. 570, Jan. 2007, pp. 17–46. https://doi.org/10.1017/S0022112006003156

[33] Al-Am, J., Clair, V., Giauque, A., Boudet, J., and Gea-Aguilera, F., "A Parametric Study on the LES Numerical Setup to Investigate Fan/OGV Broadband Noise," *International Journal of Turbomachinery, Propulsion and Power*, Vol. 6, No. 2, 2021, p. 12. https://doi.org/10.3390/ijtpp6020012

[34] Boudet, J., Monier, J.-F., and Gao, F., "Implementation of a Roughness Element to Trip Transition in Large-Eddy Simulation," *Journal of Thermal Science*, Vol. 24, No. 1, 2015, pp. 30–36. https://doi.org/10.1007/s11630-015-0752-8

[35] Lewis, D., Moreau, S., Jacob, M. C., and Sanjosé, M., "Large Eddy Simulation of the ACAT1 Fan Stage for Broadband Noise Prediction," *Journal of Sound and Vibration*, Vol. 565, Oct. 2023, Paper 117888. https://doi.org/10.1016/j.jsv.2023.117888

[36] Hanson, D. B., "Theory for Broadband Noise of Rotor and Stator Cascades with Inhomogeneous Inflow Turbulence Including Effects of Lean and Sweep," NASA CR-2001-210762, 2001.

[37] Posson, H., Roger, M., and Moreau, S., "On a Uniformly Valid Analytical Rectilinear Cascade Response Function," *Journal of Fluid Mechanics*, Vol. 663, Nov. 2010, pp. 22–52. https://doi.org/10.1017/S0022112010003368

[38] Posson, H., Moreau, S., and Roger, M., "On the Use of a Uniformly Valid Analytical Cascade Response Function for Fan Broadband Noise Predictions," *Journal of Sound and Vibration*, Vol. 329, No. 18, 2010, pp. 3721–3743. https://doi.org/10.1016/j.jsv.2010.03.009

[39] Glegg, S. A. L., "Broadband Noise from Ducted Prop Fans," *15th Aeroacoustics Conference*, AIAA Paper 1993-4402, 1993. https://doi.org/10.2514/6.1993-4402

[40] Amiet, R. K., "Noise Due to Turbulent Flow Past a Trailing Edge," *Journal of Sound and Vibration*, Vol. 47, No. 3, 1976, pp. 387–393. https://doi.org/10.1016/0022-460X(76)90948-2

[41] Roger, M., and Moreau, S., "Back-Scattering Correction and Further Extensions of Amiet's Trailing-Edge Noise Model. Part 1: Theory," *Journal of Sound and Vibration*, Vol. 286, No. 3, 2005, pp. 477–506. https://doi.org/10.1016/j.jsv.2004.10.054

[42] Liepmann, H. W., and Laufer, J., "On the Spectrum of Isotropic Turbulence," Technical Note 2473, National Advisory Committee for Aeronautics, California Inst. of Technology, Nov. 1951.

[43] Santana, L. D., Christophe, J., Schram, C., and Desmet, W., "A Rapid Distortion Theory Modified Turbulence Spectra for Semi-Analytical Airfoil Noise Prediction," *Journal of Sound and Vibration*, Vol. 383, Nov. 2016, pp. 349–363. https://doi.org/10.1016/j.jsv.2016.07.026

[44] Gea-Aguilera, F., "Aerodynamic and Aeroacoustic Modelling of Engine Fan Broadband Noise," Ph.D. Dissertation, Univ. of Southampton, England, U.K., 2017.

[45] Jurdic, V., Joseph, P., and Antoni, J., "Investigation of Rotor Wake Turbulence Through Cyclostationary Spectral Analysis," *AIAA Journal*, Vol. 47, No. 9, 2009, pp. 2022–2030. https://doi.org/10.2514/1.36728

[46] Ganz, U. W., Joppa, P. D., Patten, T. J., and Scharpf, D. F., "Boeing 18-Inch Fan Rig Broadband Noise Test," NASA CR-1998-208704, 1998.

[47] Pope, S. B., *Turbulent Flows*, Cambridge Univ. Press, Cambridge, 2000. https://doi.org/10.1017/CBO9780511840531

[48] Gea-Aguilera, F., Gill, J., and Zhang, X., "On the Effects of Fan Wake Modelling and Vane Design on Cascade Noise," *Journal of Sound and Vibration*, Vol. 459, Oct. 2019, Paper 114859. https://doi.org/10.1016/j.jsv.2019.114859

[49] Gea-Aguilera, F., Karve, R., Gill, J., Zhang, X., and Angland, D., "On the Effects of Anisotropic Turbulence on Leading Edge Noise," *Journal of Sound and Vibration*, Vol. 495, March 2021, Paper 115895. https://doi.org/10.1016/j.jsv.2020.115895

[50] Rozenberg, Y., Robert, G., and Moreau, S., "Wall-Pressure Spectral Model Including the Adverse Pressure Gradient Effects," *AIAA Journal*, Vol. 50, No. 10, 2012, pp. 2168–2179. https://doi.org/10.2514/1.J051500

[51] Salze, É., Bailly, C., Marsden, O., Jondeau, E., and Juvé, D., "An Experimental Characterisation of Wall Pressure Wavevector-Frequency Spectra in the Presence of Pressure Gradients," *20th AIAA/CEAS Aeroacoustics Conference*, AIAA Paper 2014-2909, 2014. https://doi.org/10.2514/6.2014-2909

[52] Goody, M., "Empirical Spectral Model of Surface Pressure Fluctuations," *AIAA Journal*, Vol. 42, No. 9, 2004, pp. 1788–1794. https://doi.org/10.2514/1.9433

[53] Efimtsov, B. M., "Characteristics of the Field of Turbulent Wall Pressure Fluctuations at Large Reynolds Numbers," *Soviet Physics Acoustics*, Vol. 28, No. 4, 1982, pp. 289–292.

[54] Munjal, M. L., *Acoustics of Ducts and Mufflers with Application to Exhaust and Ventilation System Design*, Wiley, New York, 1987.

[55] Tyler, J., and Sofrin, T., "Axial Flow Compressor Noise Studies," Society of Automotive Engineers Transactions, Vol. 70, Jan. 1962, pp. 309–332. https://doi.org/10.4271/620532

P. G. Tucker
Associate Editor